Coherent bremsstrahlung with the scintillating fiber detector of the BGO-OD tagging system

Master Arbeit in Physik

von
Björn-Eric Reitz

angefertigt am
Physikalischen Institut der
Rheinischen Friedrich-Wilhelms-Universität Bonn

vorgelegt der
Mathematisch-Naturwissenschaftlichen Fakultät der
Rheinischen Friedrich-Wilhelms-Universität Bonn

Oktober 2015

1. Gutachter: **Prof. Dr. Hartmut Schmieden**

2. Gutachter: **Prof. Dr. Philip Cole**

Contents

Was einmal gedacht wurde, kann nicht mehr zurückgenommen werden.

Möbius in Friedrich Dürrenmatts "'Die Physiker"'

1 Introduction

In the year 1933 Otto Stern discovered, that the magnetic moment of the proton is larger than it should be for a point-like particle[FS33][ES33]. It was possible to validate this result in further experiments. Therefore the evidence was found, that the proton is not an elementary particle but it possesses a substructure. For several years an explanation was searched. In 1964 Murry Gell-Mann[GE64] and, independently, George Zweig[ZW64] succeeded in delivering a model for the substructure via the "quark hypothesis". Through the postulation of constituents with spin 1/2 (called quarks) that are existing in three different flavors (up,down and strange), the systematical classification of the known baryons and mesons, called the particle zoo, was possible for the first time. The mathematical background for this description is based on the SU(3) group and was mainly performed by Yuval Ne'eman[YU61]. Experiments with deep-inelastic lepton scattering later delivered the needed experimental confirmations for the quark hypothesis (Bjorken scaling[BJ69], Callan-Gross relation[CG69]). The interaction between the quarks is described by the theory of quantum-chromo-dynamics (QCD).

Quarks are confined in a meson or baryon by the effective potential mediated by the gluon field and the residual of this field, the strong force, is thought to be mediated by mesons. To take this a step further, the 3 quark model can be extended to see these systems as "hadronic molecules". These are quasi bound baryon-meson states, for example in the *cloudy bag model*[CH74] the hadron is described by a three quark core surrounded by a pion cloud, or meson-meson bound states. To find such multi-quark states as evidences for this theory, many experiments are performed nowadays. First results for the baryon-meson bound state were recently achieved at LHCb at CERN[LHCb15]. The first meson-meson bound state could be the X(3872) particle observed in 2003 by the Bell experiment [Be03].

Also the experiment BGO-OD[1] settled in Bonn [BGO] was constructed for this purpose. Because the hadronic molecules are thought to be only lightly bound by remnants of the strong force, the momentum transferred to the system needs to be kept small. For BGO-OD this means, that one finale state particle, mainly a meson, needs to take over the initial momentum. Therefore this particle has a very high momentum in forward direction whereas the produced hadronic system decays nearly in rest. To fit to this special kinematic, the BGO-OD experiment contains a central detector supplemented by a forward spectrometer.
The BGO-OD experiment makes use of a real photon beam to produce hadronic excitation via photoproduction. The photon beam is produced from an electron beam by bremsstrahlung. Since this leads to a continuous energy distribution the energy of a photon producing a hadronic reaction is not known a priori, but can be determined by tagging the electron beam. The energy resolution of the tagging system limits the investigation of e.g. the η' analysis or the systematical error on the determination of the degree of linear polarization of the photon beam. Reducing the systematical error is crucial to accurately determine polarization observables.

This master thesis is concerned with the setup of a scintillating plastic fiber detector ARGUS[2], in cooperation with Stefan Alef [Al15], for the tagging system to improve the energy resolution.
First, simulations were performed to understand the detectors behavior and how different parameters influence the results. With this gained information a first prototype was constructed and tested it in a short beam time. The results helped to improve the prototype to get an easier final concept with better performance. At the end the final setup could be tested and the detectors properties were determined. With the data collected with ARGUS, a small analysis of the beam asymmetry Σ in π^0 photoproduction was performed. The values for the polarization, obtained from the beam asymmetry, are used for a consistency check of values obtained by calculations using the tagger/ARGUS spectrum. The second goal was to investigate the impact of the improved energy resolution on the systematic error for the determination of the degree of polarization using these calculations.

The thesis will begin with an overview of the BGO-OD experiment in chapter 2. The next chapter 3 treats the physics of bremsstrahlung which is necessary to produce polarized photons. The tagging system will then be presented in chapter 4. The new scintillating fiber detector ARGUS and its results are the main content of chapter 5. The last chapter will show the results of the beam asymmetry analysis in $\pi^0 p$ photoproduction.

[1] BGO is for the scintillating material $\mathbf{Bi}_4\mathbf{Ge}_3\mathbf{O}_{12}$ in the main detector, OD results from the use of an **o**pen **d**ipolmagnet.
[2] the name is inspired by the mythological creature Argos which had a high amount of eyes always awake

2 The BGO-OD experiment

The goal of the BGO-OD experiment is to investigate the structure of excited mesonic decays, especially in respect to a molecular structure. This is done by impinging an photon beam on a liquid hydrogen or deuterium target. Due to the special kinematics, the experiment consists of two parts. An overview of the experiment is shown in figure 2.1.

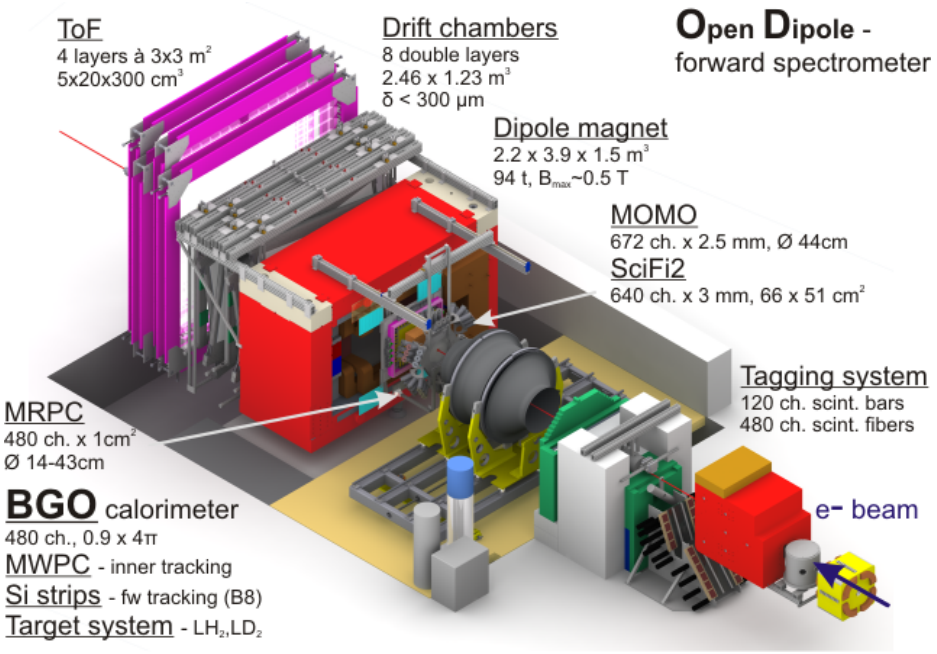

Figure 2.1: Schematic setup of the BGO-OD experiment. The electron beam of ELSA enters from the bottom right.

The main part of the central detector region is the BGO ball. An electromagnetic calorimeter to detect the charged and uncharged final states of the reactions. The BGO ball counts 480 $Bi_4Ge_3O_{12}$ scintillating crystals covering the solid angle range of 0.9 - 4π. It provides good energy and timing information, and a limited spacial resolution. The limitation in spacial resolution results from the needed extend of the crystals used for the BGO. The charge information is accessed via dE/dx measurements by a plastic scintillator barrel (short: barrel) consisting of 32 scintillating counters cylindrical orientated around the target. Between the target and the barrel two layers of MWPC's[3] are planned. Each of them consists of two coaxial cylindrical cathodes together with one anode, made of wires, along the beam axis. This setup will serve for inner particle tracking.

The forward spectrometer is needed to detect and identify particles with high momenta.
To reconstruct the particle tracks one makes use of two scintillating fiber detectors, MOMO[4] and SciFi2[5], in front of a large open dipole magnet and eight drift chambers behind the magnet. MOMO consists of 672 channels covering an active area with 44cm radius around the beam axis. The 640 channels of SciFi2 covering an area of $66 \cdot 51\ cm^2$. It has a time resolution of around 2ns and an acceptance region of $\pm 10°$ in horizontal and $\pm 8°$ in vertical direction.
Each drift chamber contains a double layer of hexagonal drift cells, so that each particle track will hit at least two drift cells in each chamber it passes. Furthermore only two chambers have the same orientation. Two for measuring the x- coordinate, two for the y-coordinate and 2 tilted by 9° against vertical for crosschecks.
The last part of the forward spectrometer are the Time-of-flight (short: ToF) walls. They are made of 48 large 3000 mm x 115 mm x 30 mm plastic scintillator bars in 4 layers. In each layer the bars are stacked next to each other covering the polar angle range up to 12 degrees. As the name already predicts they are used to measure the time, charged or uncharged particles, needed to travel the 5 m distance between target and ToF.

[3] **M**ulti-**w**ire **p**roportional **c**hamber
[4] **M**onitor **o**f **M**esonic **O**bservables
[5] **Sci**ntillating **Fi**bers

This is then used together with the particle track for particle identification.

The photons needed for the photopoduction of the final states are produced from electrons delivered by the three stage electron accelerator ELSA (see fig. 2.2). ELSA can provide unpolarized and polarized electrons up to an energy of 3.5GeV.
The extracted electrons impinge on either an amorphous or crystal radiator producing unpolarized or linear polarized photons through bremsstrahlung. Furthermore it is possible to produce circularly polarized photons by using the polarized electrons from ELSA on an amorphous radiator. The tagging system of the BGO-OD experiment is a crucial part, since the photon energy is not known a priori due to the characteristics of bremsstrahlung presented in the next chapter. A detailed description of the present tagging system before this thesis will be given in chapter 4.
For further information on the BGO-OD experiment e.g. [BGO] can be used.

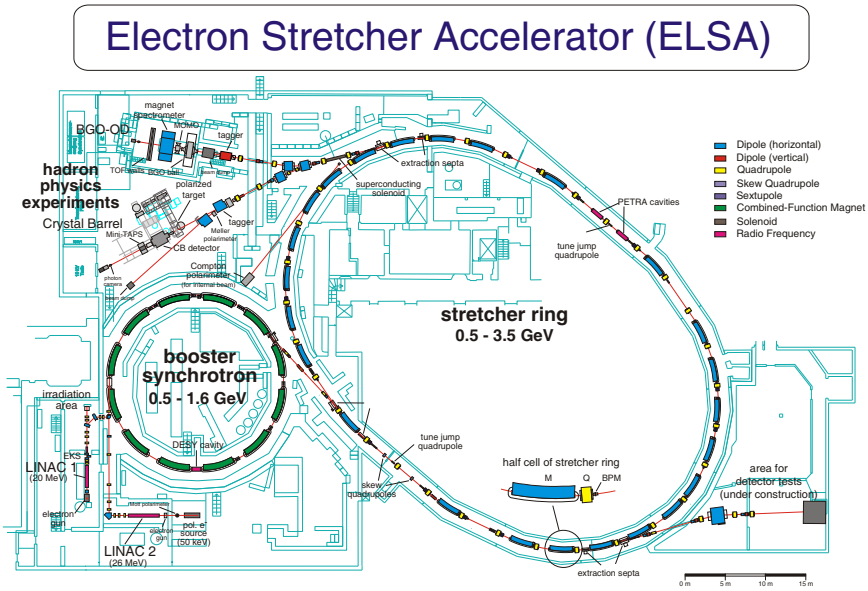

Figure 2.2: Schematic setup of the electron accelerator ELSA in Bonn.

3 Bremsstrahlung

For the photoproduction of mesons photons are needed. For the BGO-OD experiment they are produced via bremsstrahlung. In the following chapter the physical background for this process will be given. First some general remarks to the kinematics. Then the distinction between incoherent and coherent bremsstrahlung will be annotated. Some characteristics of both will be shown.

3.1 General kinematics

One reason for electrons to loose energy if they pass matter is bremsstrahlung. It is a result of the electrons interaction with the coulomb field of the atomic core or a shell electron.

$$e^- + N \rightarrow e^- + N + \gamma \tag{3.1}$$

The electron is negatively accelerated during this process and emitts one or more real photons. Due to momentum conservation of the four-momentum the scattering partner has to take a defined recoil momentum:

$$E_0 = T + E + k \tag{3.2}$$

$$\vec{p_0} = \vec{q} + \vec{k} + \vec{p} \tag{3.3}$$

with:

$E_0, \vec{p_0}$	:	energy and momentum of incoming electron
$E, \vec{p}$	:	energy and momentum of outgoing electron
$k, \vec{k}$	:	energy and momentum of bremsstrahlungs photon
$T, \vec{q}$	:	recoil energy and momentum of scattering partner.

In the following consideration the kinetic energy T of the recoil can be neglected because it is small compared to the rest energy for momenta we investigate here. Due to rotational symmetry of the bremsstrahlungs process one can divide it by transverse and longitudinal components. The definition and orientation of the different components is shown in figure 3.1.

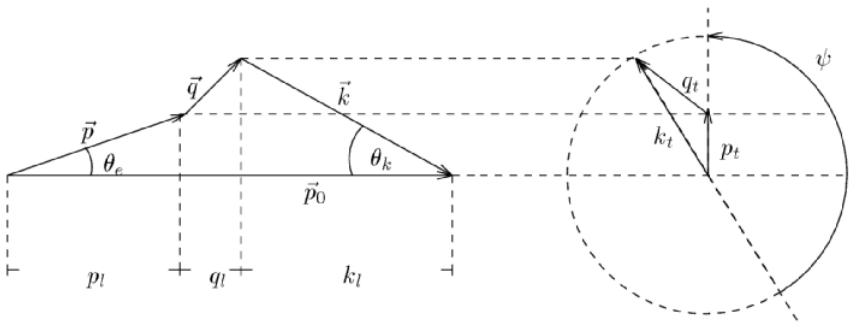

Figure 3.1: Shown is the definition of longitudinal (l) and transverse (t) components relative to the direction of the incoming electron for the bremsstrahlungs process. Figure taken from [Tim69].

Using some geometrical rules one can follow that

$$q_l = p_0 - p\cos\Theta_e - k\cos\Theta_k. \tag{3.4}$$

With the, due to high momenta, allowed simplification that the photon is emitted in direction of the electron the transverse component and the angles Θ_e and Θ_k vanish plus the longitudinal component of the momentum is minimal (mostly denoted with δ):

$$q_l^{min} = p_0 - p - k \stackrel{!}{=} \delta. \tag{3.5}$$

Since we use primary electron energies of a few GeV furthermore the simplification

$$p = \sqrt{E^2 - 1} = E - \frac{1}{2}E \tag{3.6}$$

is justified and leads then together with the relative photon energy

$$x = \frac{k}{E_0} \tag{3.7}$$

to an expression for δ

$$\delta = \frac{1}{2E_0}\frac{x}{1-x}. \tag{3.8}$$

In case of constant primary energies this means that with increasing photon energies the longitudinal momentum transfer increases. Nonetheless δ is small compared to the other momenta involved. For $E_0 = 2 \cdot 10^3$ and $x = 0.3$ one gets $\delta = 1.07 \cdot 10^-4$ compared to $p_0 = 2 \cdot 10^3$ [Tim69].
Replacing the photon angle trough the characteristic angle[6] $\Theta_c = \frac{m_e}{E_0}$ of bremsstrahlung one gets an approach for the maximal momentum transfer:

$$q_l^{max} \approx \frac{1}{E_0}\frac{x}{1-x} = 2\delta \tag{3.9}$$

Similar thoughts for the transverse component lead then to the kinematically allowed region for the bremsstrahlungs process

$$\delta \leq q_l <\approx 2\delta \tag{3.10}$$

$$0 \leq q_t <\approx 2x. \tag{3.11}$$

Precise calculations like done in [Tim69] lead to the final setup for the allowed cinematic region:

$$\delta + \frac{q_t^{max}}{2E_0} \leq q_l <\approx \frac{\delta}{x} \tag{3.12}$$

$$0 \leq q_t <\approx 1. \tag{3.13}$$

One important fact is that there is a sharp lower bound for the momenta. The allowed region in total was called by [Ue56] **pancake** due to its geometry. Figure 3.2 shows this region for both cases, the approximation and the exact solution.

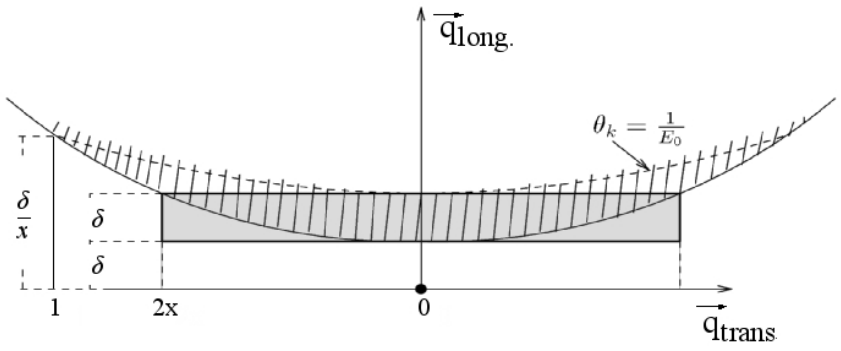

Figure 3.2: The kinematically allowed region for the momentum transfer. The region which follows from approximation is completely filled with gray the exact result is shaded. Because $q_l << q_t$ the q_t-axis is clinched. Figure taken from [Tim69].

[6] the angle is defined as the opening angle of a cone in momentum direction of the primary electron that contains half of the emitted bremsstrahlungs photons

3.2 Incoherent bremsstrahlung

Incoherent bremsstrahlung is the fundamental process, underlying even the coherent bremsstrahlung which is produced in crystals (see chapt. 3.3.1). The incoherent bremsstrahlung can be observed clearly in amorphous radiators. Since the recoil momentum is carried by each scattering center seperately, no discrete scattering plane between the incoming electron and the emitted photon is preferred. This then leads to a randomly orientated electric field vector of the photon, meaning that the photon is unpolarized.

3.2.1 Cross section

In general the cross section for scattering processes is described by

$$\sigma = \frac{|M_{if}|}{\text{time} \cdot \text{particle flux}} \tag{3.14}$$

where $|M_{if}|$ denotes the matrix element giving the possibility for a scattering process. If one treats the atom as a point like charge , meaning that it is described by

$$V(\vec{q}) = -\frac{4 \cdot \pi \cdot Z \cdot e}{\vec{q}^2} \tag{3.15}$$

in the momentum frame and using the Born approximation[7], one gets

$$d\sigma \propto |V(\vec{q})|^2 \propto \frac{1}{|\vec{q}|^4}. \tag{3.16}$$

This means then, the smaller $\vec{q}$, the cores recoil momentum, gets the larger the contribution to the bremsstrahlung cross section gets. Doing some proper calculations like done in [Hei54] one first will get the Bethe-Heitler-cross section. Because only the energy spectrum should be investigated, an integration overall electron emission angles and photon angles Θ_k will finally lead to the spectral distribution of incoherent bremsstrahlung [Lan86].

$$d\sigma_{B.H} = 4Z^2 \alpha a_0 \frac{dk}{k} \frac{E}{E_0} \left[\frac{E_0}{E} + \frac{E}{E_0} - \frac{2}{3} \right] \left[\ln\left(\frac{2E_0 E}{k} \right) - \frac{1}{2} \right]. \tag{3.17}$$

In first approximation one notices the $1/k = 1/E_\gamma$ dependence of the spectrum

3.3 Coherent bremsstrahlung

Coherent bremsstrahlung is accessible if one uses radiators with a crystalline structure. In such a radiator the scattering partners are periodically positioned. Due to this special orientation the bremsstrahlungs contribution of the several scattering partners can interfere constructively. The underlying kinematics are the same as for the incoherent process presented in 3.2 with the small difference that the recoil momentum is distributed to more than one scattering partner. Therefore the name "coherent". The resulting modifications in the cross section will be presented below.

3.3.1 Kinematics in coherent bremsstrahlung

To investigate the momentum transfer, it is helpful to go from the crystal lattice itself to the reciprocal one as coordinate system. A reciprocal lattice vector describes a group of parallel planes in the coordinate space. Every single component of this vector is given by the Miller indicies [**?**]. If the electrons momentum should be taken by the whole crystal, the Laue-Bragg condition

$$\vec{q} = n \cdot \vec{g} \tag{3.18}$$

must be fulfilled. It means that only momentum transfers $\vec{q}$ can be taken over by the crystal that are a integer number n times the reciprocal lattice vector $\vec{g}$. Equation 3.16 shows that small momentum transfers, described by smaller miller indicies, are the dominant distribution of the cross section. As already mentioned in the incoherent case the momentum transfer must be in the same allowed region (pancake 3.2) for the coherent case. Furthermore it is possible, by precise orientation of the crystal, to determine the reciprocal lattice vector inside the pancake. Because of the selection of discrete recoil momenta also the scattering plane between the momentum vector of electron and proton are fixed. This leads to a fixed orientation of the electric field vector of the photon and therefore a net linear polarization.

[7] for extremely relativistic electrons $Z \cdot \alpha << 1$ holds. α is the fine structure constant.

3.3.2 Cross section of coherent bremsstrahlung

Crystals have defects in the lattice structure. Furthermore there is always an underlying, random orientated thermic motion of the scattering centers. Such processes increase the anyway existing incoherent bremsstrahlung in crystals. Therefore the total cross section of a crystal can be described in first approximation by

$$d\sigma_{\text{crystal}} = d\sigma_{\text{coh}} + d\sigma_{\text{incoh}}. \tag{3.19}$$

The reasons for the different contributions will be presented in the following part.

The Debye-Waller factor
Thermic motion leads to a lowered momentum transfer to the lattice. This then leads to a lowered contribution to the coherent spectrum. The Debye-Waller factor describes the strength of this effect. The factor is given by the function

$$f\left(q^2\right) = \exp -A\left(T\right) q^2. \tag{3.20}$$

The function A, dependent of temperature T, describes the mean thermic displacement of the atoms. It is defined by

$$A\left(T\right) = \frac{3m_e^2c^2}{4Mk_b\Theta}\left[1 + 4 \cdot \frac{T}{\Theta} \cdot \Phi\left(\frac{\Theta}{T}\right)\right], \tag{3.21}$$

with M the mass of a atom, m_e mass of a electron, the Boltzmann constant k_B and the Debye temperature of the crystal Θ. Furthermore it contains the Debye function which is given by

$$\Phi\left(\frac{\Theta}{T}\right) = \frac{T}{\Theta}\int_0^{\Theta} \frac{T'dT'}{c^{T'} - 1}. \tag{3.22}$$

The larger the temperature, the smaller the Debye-Waller factor gets because $A\left(T\right)$ is getting larger.
If one is interested in a high coherent cross section one needs crystals with high Debye temperatures. This is therefore the reason for the BGO-OD experiment to use a diamond radiator. Diamond has the highest Debye temperature with $\Theta = 2230\text{K}$ compared to e.g. beryllium ($\Theta = 1160\text{K}$) or silicate ($\Theta = 640\text{K}$).

The diffraction factor
Compared to the incoherent case, in the coherent bremsstrahlungs process more than one atom (N) contribute. Therefore the simple coulomb potential must be replaced by the lattice potential. The amplitude of incoming and outgoing particle wave can then be calculated by summation of the contributions of the several scattering centers. The differential cross section is the absolute value squared of these amplitudes:

$$d\sigma_N\left(\vec{q}\right) = D\left(\vec{q}\right) \cdot d\sigma\left(\vec{q}\right). \tag{3.23}$$

It is therefore the same as the Bethe-Heitler cross section for a process with one scattering center multiplied by a factor $D\left(\vec{q}\right)$. The factor is called diffraction factor and is given for a crystal radiator by [Tim69]

$$D\left(\vec{q}\right) = \left(\frac{2\pi}{a}\right)\sum_{h_{kl}}\prod_{k=1}^{3} N_k \cdot \delta\left(q_k - \frac{2\pi h_{kl}}{a}\right), \tag{3.24}$$

with a the lattice constant. The delta function in the diffraction factor only allows momentum transfers q_k that are represented by a reciprocal lattice vector.

The structure factor
The structure factor $S\left(\vec{g}\right)$ describes the effect of destructive interference of the emitted waves produced by different scattering centers caused by the lattice. For a diamond this is for a reciprocal lattice vector $\vec{g} = h\vec{b_1} + k\vec{b_2} + l\vec{b_3}$ given by [Tim69] as

$$\begin{aligned}
\left|S\left(\vec{g}\right)\right|^2 &= 64, \text{if h,k,l even and (h + k + l)/4 integer} \\
\left|S\left(\vec{g}\right)\right|^2 &= 32, \text{if h,k,l odd} \\
\left|S\left(\vec{g}\right)\right|^2 &= 0, \text{else}
\end{aligned}$$

The several lattice points must be weighted by this structure factor, so that for a diamond (8 atoms as base) following participation for the differential cross section holds

$$d\sigma_N\left(\vec{q}\right) = \left(\frac{2\pi}{a}\right)\frac{N}{8}\left[\sum_{\vec{g_v}}\left|S\left(\vec{g}\right)\right|^2 \cdot \delta\left(\vec{q}-\vec{g_v}\right)\right] \cdot d\sigma\left(\vec{q}\right), \tag{3.25}$$

with the reciprocal lattice vector $\vec{g_v}$.

Therefore in total the differential cross section for a diamond is given by

$$d\sigma_{\text{crystal}} = \left[D\left(\vec{q}\right) f\left(q^2\right) + \left(1 - f\left(q^2\right)\right) N\right] d\sigma_{\text{B.H.}}. \tag{3.26}$$

Figure 3.3 shows the cross section for bremsstrahlung off an amorphous radiator (blue) and off a diamond crystal (black). Clearly visible is the approximate $1/E_\gamma$ behavior of the incoherent process which, due to the reasons described above, is also visible for the diamond. Furthermore, in the diamond spectrum, peaks are present due to the increased cross section in coherent bremsstrahlung. If the complete spectrum is normalized to the incoherent one, only the coherent contribution is visible (red curve). The sharp drop of the coherent peaks (coherent edge) is due to lattice vectors leaving the kinematically allowed region (pancake, equations 3.12 and 3.13). The equations used to determine the cross section make use of some simplifications. Figure 3.4 shows the spectra with experimental influences. Due to multiple scattering of the electrons in the radiator or divergence of the electron beam the coherent peaks are blurred. The larger the photon energy gets the broader and smaller in amplitude the peaks get. Therefore one gets the possibility to distinguish which peak corresponds to which lattice vector.
The photon production via bremsstrahlung is a crucial part of the BGO-OD experiment. But due to the continuity of the photon spectrum, even for a fixed incoming electron energy, the energy of a photon reacting with the target is not known a priori. To overcome this problem the very important tagging system was constructed for the BGO-OD experiment.

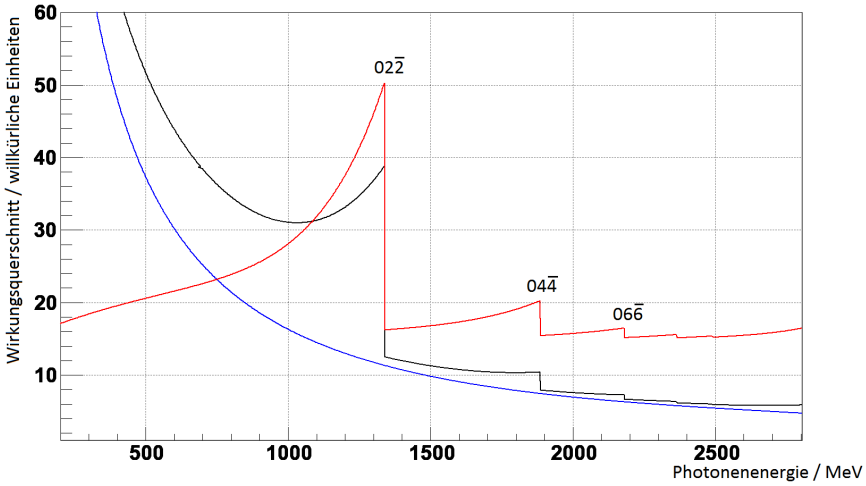

Figure 3.3: Cross section in arbitrary units for bremsstrahlung off an amorphous radiator (blue) and off a diamond (black). The red curve describes the coherent contribution to the cross section for the diamond.

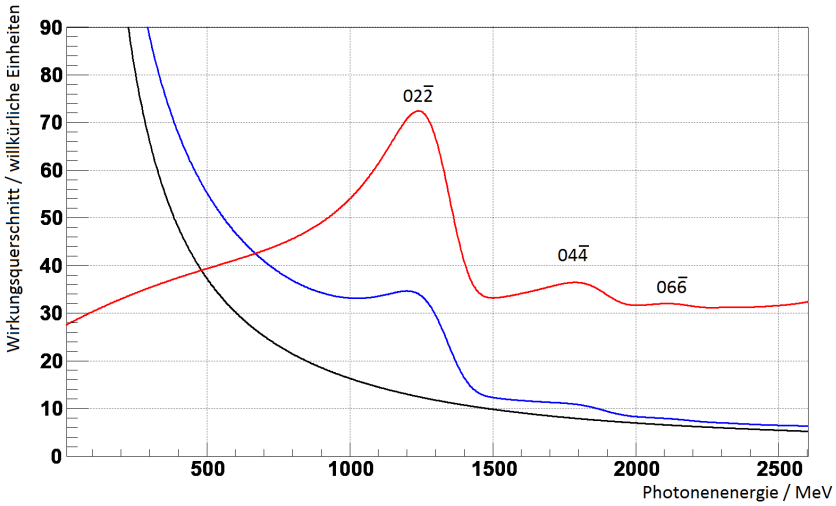

Figure 3.4: By experimental influences corrected cross section in arbitrary units for bremsstrahlung off an amorphous radiator (blue) and off a diamond (black). The red curve describes the coherent contribution to the cross section for the diamond.

4 The photon tagging system

The energy of the real photons in the bremsstrahlungs spectrum must be determined. This is accomplished using a photon tagging system (short:tagger). The tagging system for the BGO-OD experiment was setup by Andreas Bella [Be].

A schematic overview of the tagging principle is presented in figure 4.1.

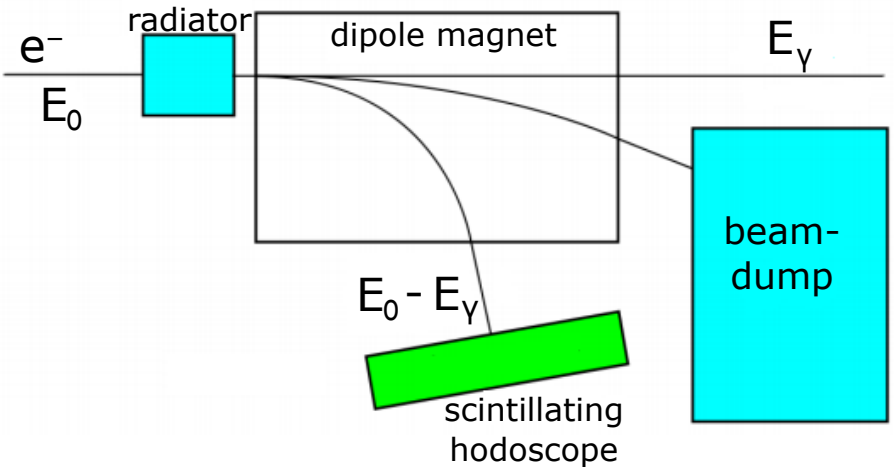

Figure 4.1: Schematic setup of a tagging system.

Electrons entering from the left will loose energy due to photon production in the radiator. For the energies holds

$$\begin{aligned} E_0 &= E + E_\gamma \\ \rightarrow E_\gamma &= E_0 - E \end{aligned} \tag{4.1}$$

where E_0 is the electron energy provided by the accelerator, E_γ the photon energy and E the electron energy measured after the bremsstrahlungs process. Therefore a determination of E is needed to obtain the photon energy E_γ. For this purpose a dipole magnet is positioned behind the radiator deflecting the post-bremsstrahlung electrons. For the electron momentum holds $p_e = e \cdot B \cdot r$ which leads to an energy dependent separation of the scattered electron beam. The electrons are then detected by a scintillator hodoscope to determine their position and therefore their bending radius. From this one obtains the energy of the post-bremsstrahlung electrons. With equation 4.1 this finally leads to the needed photon energy.
The primary beam of the accelerator which have not undergo bremsstrahlung is not deflected in the hodoscope but into a beam dump made of lead to prevent further interactions with other parts of the experiment.

The best position for the hodoscope is in the magnets focal plane. Due to limited space between beam-dump and the magnet in the BGO-OD experiment the hodoscope is split into two parts. One part detecting scattered electrons with energies up to $E \approx 0.32 \cdot E_0$ in the focal plane and one vertical part which is used for energies up to $E \approx 0.9 \cdot E_0$. Figure 4.3 shows a schematic overview of the position for the 120 scintillators used for the hodoscope. Different sizes of the scintillators in the vertical part give the opportunity to keep a good energy resolution even for the upper part where the electrons are less spacial seperated (see figure 4.2). This also leads to use of different photomultiplier in the several regions. Namely these are ET Enerprise 9100SB in the horizontal part and the lower vertical part and Hamamatsu R7400U in the upper vertical part. The latter make use of a smaller diameter together with a lower transit time and rate stability for high rates. These high rate are an effect of the bremsstrahlungs spectrum which is discussed in chapter 3.

The energy resolution obtained by the tagger can be seen in figure 4.2. It reaches from $0.55\% E_0$ for the lower to $2.1\% E_0$ for the upper channels. The current energy resolution limits e.g the analysis of η' and methods e.g. the determination of the degree of linear polarization (chapter 6). To increase the energy resolution of

the tagging system, a new detector consisting of scintillating plastic fibers was designed and will be presented in the next chapter.

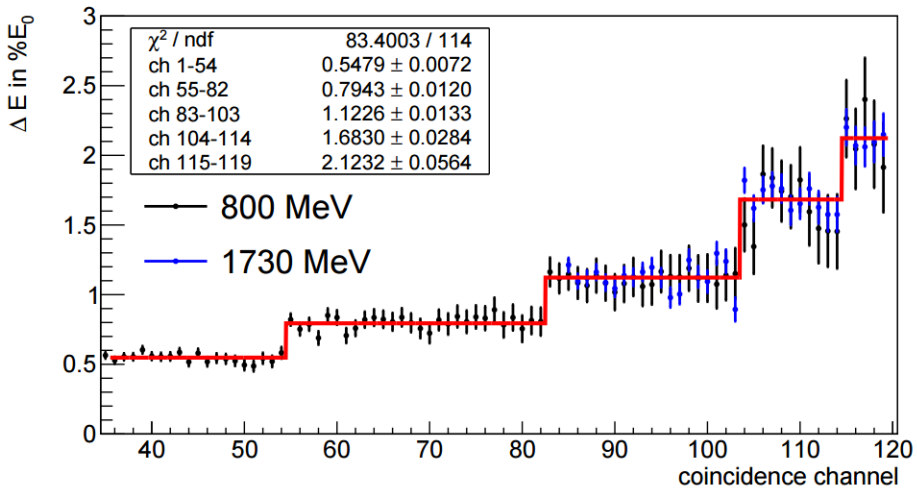

Figure 4.2: Energy resolution of tagging system. The black points were obtained using a 800MeV and the blue a 1730MeV beam.[Be]

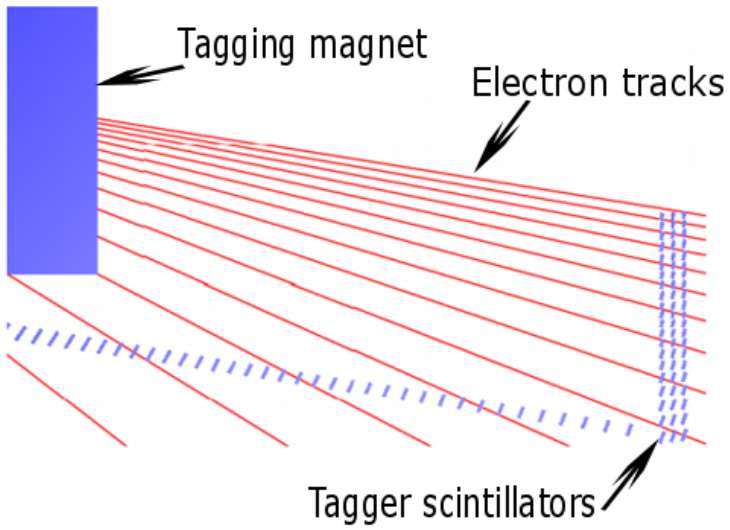

Figure 4.3: Position of tagger scintillators with respect to the dipole magnet (blue square). The red lines correspond to simulated electron tracks in steps of 200MeV.

5 ARGUS

The tagger has a limited energy resolution of about $0.55\%E_0$ to $2.1\%E_0$. For example, to decrease the systematic error in determination of the degree of linear polarization, an increase in the energy resolution is needed. Since the normal photomultiplier tubes need some space, one cannot use smaller scintillators. The way out is given by scintillating fibers (like used in SciFi2 and MOMO, chapter 2) read out via multi-anode-photomultipliers. In this chapter, first a simulated analysis will be presented followed by the physical background of the several parts that will be used for the real detector called ARGUS. The process of planning and construction will be presented. Results will be shown for each development step and finally in chapter 5.6 for the final design tested in a 3 week beamtime. All of this was done in corporation with Stefan Alef [Al15].

5.1 Requirements and simulations

The design of ARGUS should fulfill several criteria:

- increase the energy resolution in the covered energy region
- constant electron detection efficiency near 100% to make use of maximum experimental event rate
- rate stability even for high rates so that no electrons are lost
- compact design due to limited amount of space in the existing tagging system
- no impact on the existing tagging system

To test if and how it is possible to fulfill these criteria, a simulation of the detector was performed. In general there were four issues that had to be addressed:

1. Should the detector be formed of 2 or 3 layers of scintillating fibers?
2. Should the detector or parts be tilted for better efficiency and energy resolution?
3. By how much will broken fibers (or also broken photomultiplier channels) affect the overall detector resolution?
4. What is the influence of gaps (paint, glue, holding structure) between the fibers in detector resolution.

The efficiency in the simulations is defined as

$$\text{efficiency} = \frac{\text{total amount of electrons that produce a cluster with this index}}{\text{amount of electrons that produce a cluster with enough energy deposited in each fiber}}.$$

Since working with a simulation these information are easy and accurately accessible. The amount of energy needed to be deposited inside a fiber can be calculated as 170keV. More to this in chapter 5.2.1.

To understand the results a definition of a cluster is needed. Figure 5.1 shows a schematic side view along the fibers of a 3 layer setup. Each circle represents the geometrical extension of a fiber seen while looking along the fiber. Blue circles are fibers that are not hit, or where not enough energy, 170keV, is deposited. The green circles represent fibers where enough energy is deposited by the electron to produce a detectable signal. The red lines should depict the possible tracks of an electron, which could be oriented after the tagger magnet between 12° and 22° with respect to the beam line for the desired position of ARGUS, or the track of an delta electron producing a hit in an additional fiber (light blue circle).
A cluster is defined when at least 2 fibers in a allowed geometrical connection are hit. Geometrical allowed is in this way e.g.:

- fibers 4,5 and 6 are hit
- fibers 4 and 6 are hit
- fibers 4 and 5 are hit

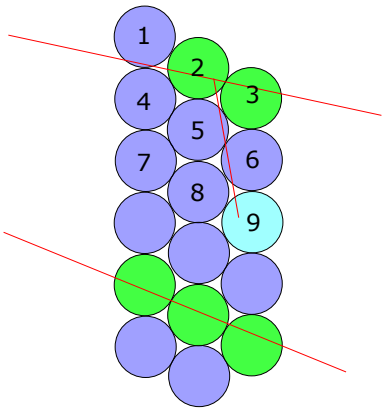

Figure 5.1: Definition of a cluster in the three layered configuration. For the meaning of the circles and lines see text.

- fibers 5 and 6 are hit
- fibers 4, 7 and 8 are hit

and so on. After these hits are put together in a cluster, the index of the cluster must be defined. In case of ARGUS each cluster gets the index of the first layer. Therefore 480 fibers correspond to 160 clusters in total. A cluster can also be larger than these 3 hits. For example the fibers 4,5,6,7 could be hit and will become a cluster with index 4. These multi-hits could happen for one thing through the production of delta electrons. If they hit fibers further away from the incident electron path these hits will not become a part of the cluster. Otherwise some low energetic background from the accelerator or other sources could produce additional hits that can be part of a cluster. This is then also the main reason why at least 2 hits must fulfill the geometric constrains to build a cluster. Else there would be a lot of background measured as real electrons. This impact of minimum cluster size of 2 is also clearly visible in the simulation results for 2 layers presented in the next chapter.

In total we used the following set of parameters for simulations:

- 2 layers of fibers tilted by 0°, 10° and 20°
- 3 layers of fibers tilted by 0°, 10° and 20°
- 2 layers of fibers tilted by 10° with 0.25mm space between the fibers
- 3 layers of fibers tilted by 0° with 0.25mm space between the fibers

All simulations were performed with either 19 broken fibers for 2 layers and 33 broken fibers for 3 layers randomly distributed but always the same. The angle setting with best results in efficiency and energy resolution were then used to simulate gaps of 0.25mm between the fibers.

5.1.1 Results of the simulations for 2 layers

Since the desired amount of available channels for the detector is limited, a simulation of 2 layers of fibers is needed. In case of 2 layers, a larger energy region could be covered than for 3 layers. This is clearly visible in the energy resolution plots for the different angles shown in figure 5.3. One can see that a smaller energy resolution than the tagger $(0.55 - 2.1\% E_0)$can be achieved for each tilting angle. The fluctuations are an effect of the broken fibers.
The other very important criterion of a high efficiency cannot be fulfilled even with a tilted detector as can be seen in figure 5.2 where only efficiencies of around 90% are achievable. In case of 0° tilting, the efficiency is higher (up to 98%) but its dependent of the cluster position. For the lower cluster indices, meaning lower photon energies, its again around 90%. The impact of broken fibers is clearly visible. The efficiency drops to about $30 - 40\%$ for clusters that contain these fibers which can be seen in every plot. This is as expected, since for two layers the failure of one fiber means that only half of the electrons can be detected.

The simulation with the gaps between the fibers shows that the overall efficiency drops by additional $3-4\%$. Notice that the maximum cluster index is lower then in the other cases because with the gaps now fewer fibers cover the same energy region.

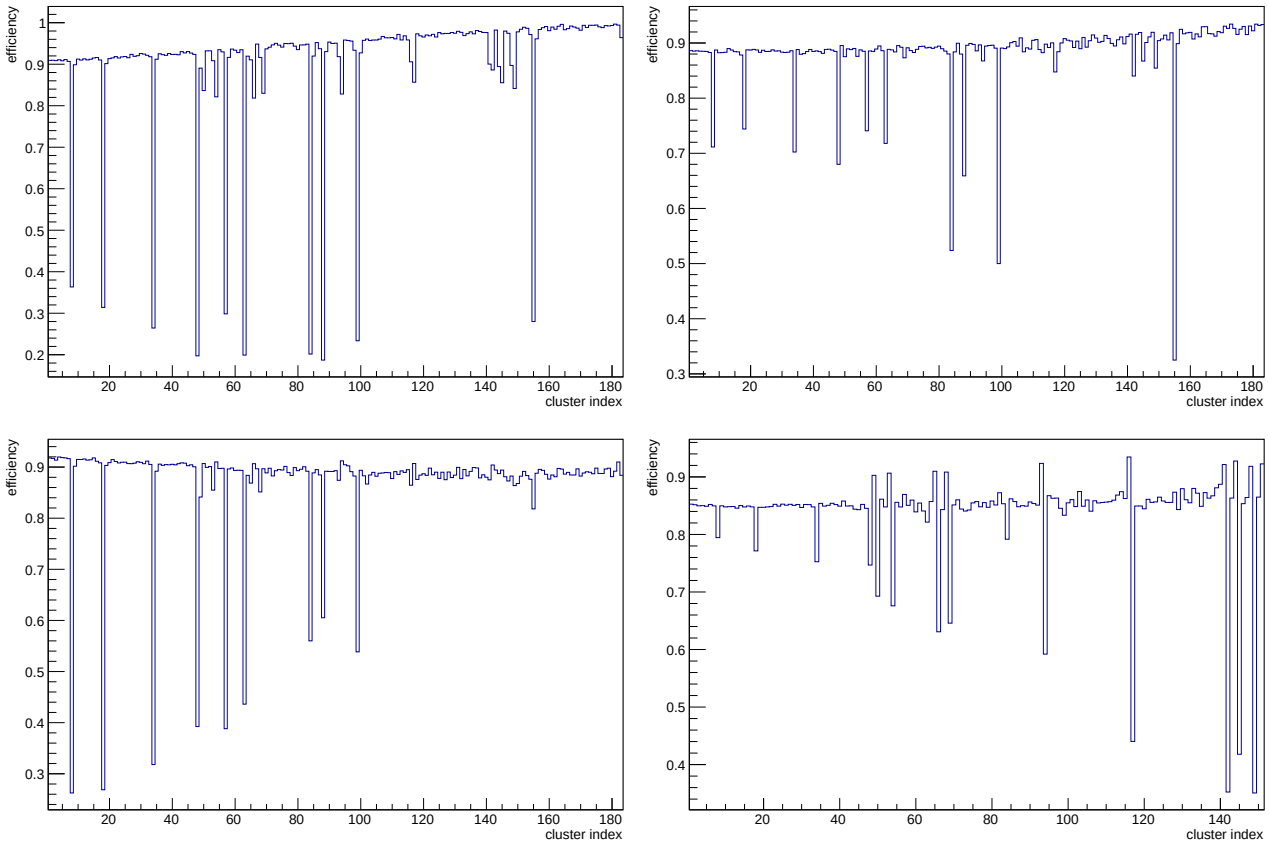

Figure 5.2: Efficiency obtained in simulations for 0° (top left), 10° (top right), 20° (bottom left) and 10° with gaps (bottom right) for 2 layers of fibers.

So all in all the simulations for 2 layers show that, as expected, the desired properties of the detector cannot be fulfilled even if one has the ability to cover the same energy region for the entire vertical tagger. This is mainly because of the fact that clusters need to have at least 2 members. If now one fiber does not register a hit, then there is no chance that the electron can produce a 2 sized cluster. These events then are not defined as a detected electron and therefore reduce the efficiency. This effect is qiute noticeable in the case of gaps between the fibers. This increases the region where no fibers are able to detect an electron. The 3 layer results presented next show that this is not the case there.

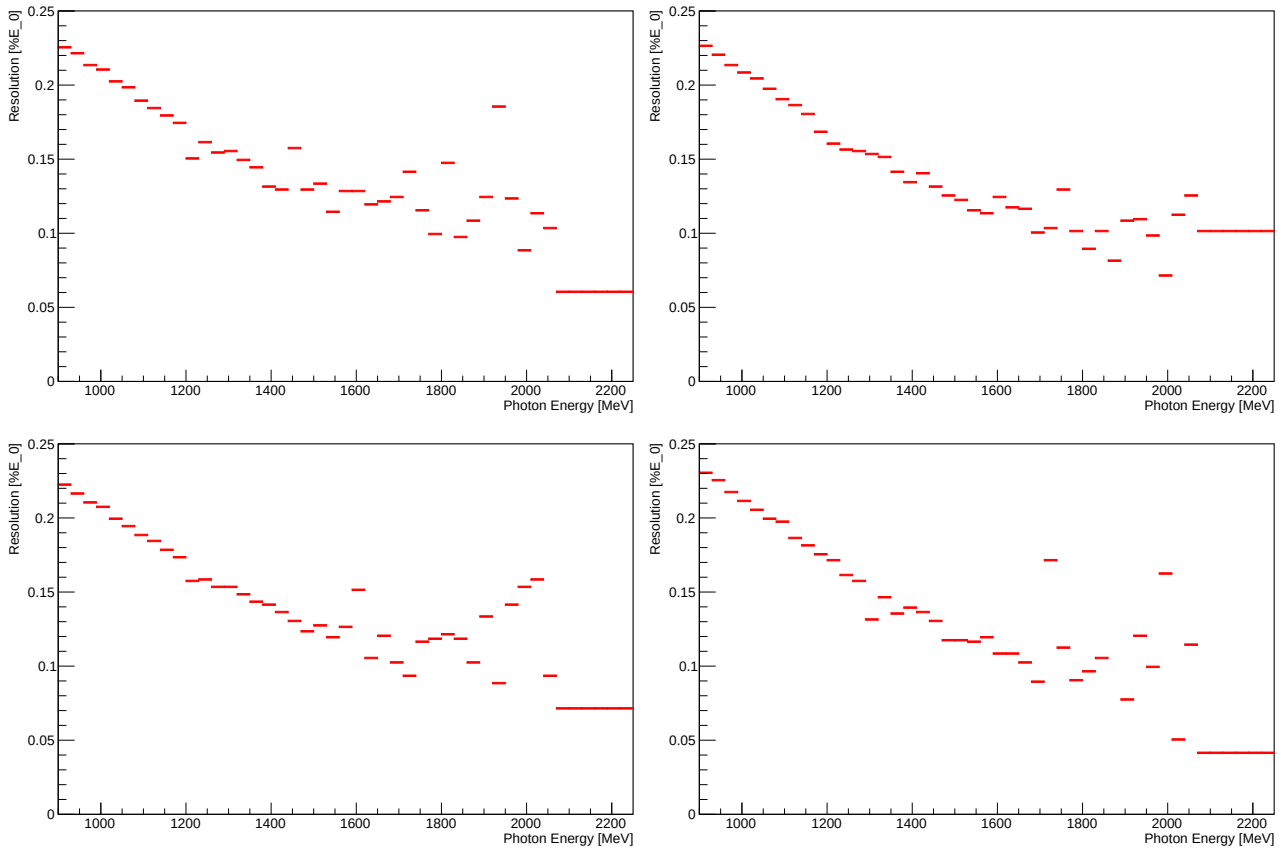

Figure 5.3: Energy resolution obtained in simulations for 0° (top left), 10° (top right), 20° (bottom left) and 10° with gaps (bottom right) for 2 layers of fibers.

5.1.2 Results of the simulations for 3 layers

The results and behavior of the two-layered configuration is not a viable option, we require the redundancy afforded by a third layer. Three layers limit the active detector region but as one can see in the figures 5.3 and 5.4 provide beneath a very good energy resolution to better than $0.22\% \cdot E_0$ and provides a nearly 100% efficiency as long as not tilted (e.g. axis goes from 0.9 to 1 for the upper left plot). The fluctuations in the energy resolution plot are less pronounced compared to the 2 layer setup since broken fibers do not have that much impact.
If tilted, the efficiency in some parts drops slightly to about 95%. These points are clearly visible as broad dips. At these points, the incoming electrons are able to pass between the active regions of adjacent fibers as one can understand looking on figure 5.1 again. In this case no cluster with at least two members can be constructed. Compared to the 2 layer design for the most cases if 2 fibers would not be enough to build a 2-sized cluster the third layer prevent the event from not being counted as real electron by detecting this electron leading to a 2-sized cluster again

Therefore to obtain a maximum of efficiency and the desired energy resolution for ARGUS, a design making use of 3 layers of scintillating plastic fibers is used.

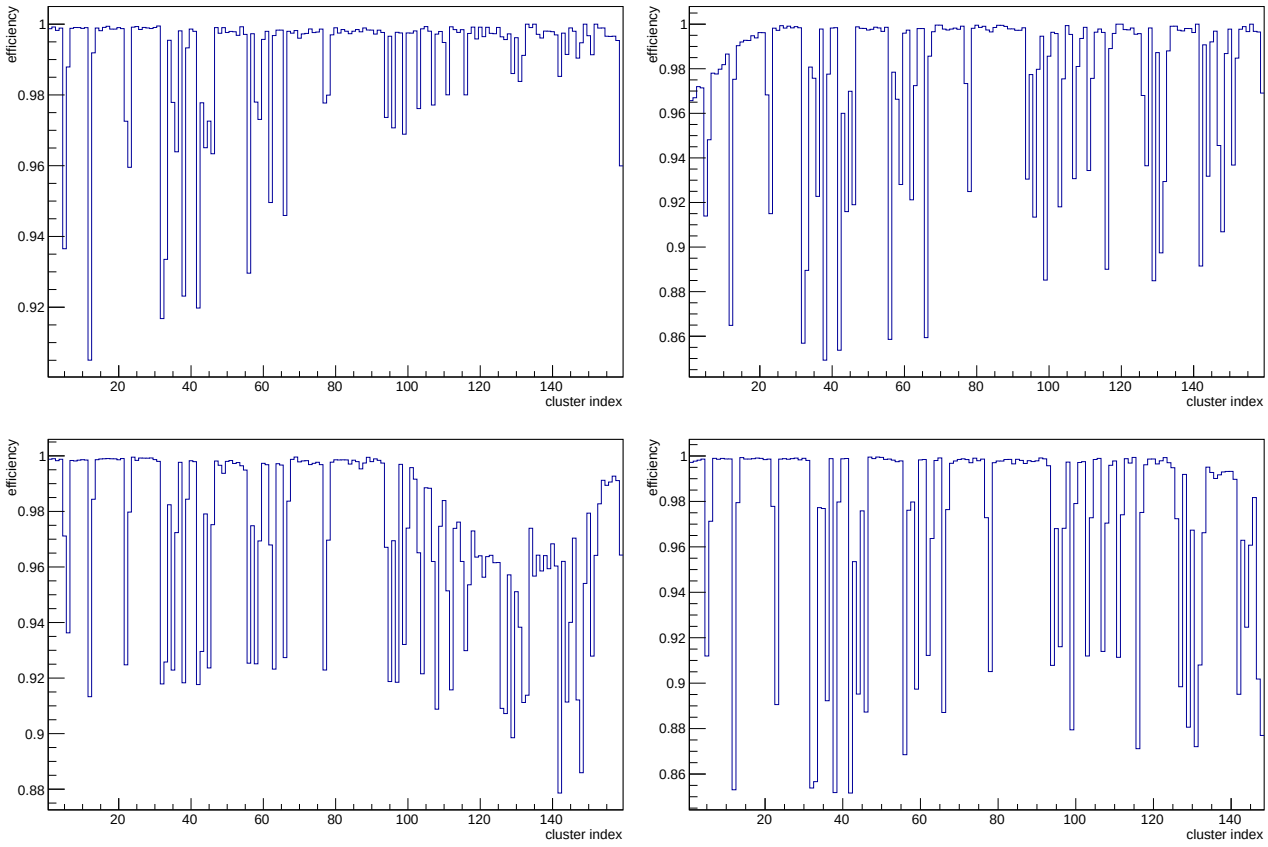

Figure 5.4: Efficiency obtained in simulations for 0° (top left), 10° (top right), 20° (bottom left) and 10° with gaps (bottom right) for 3 layers of fibers.

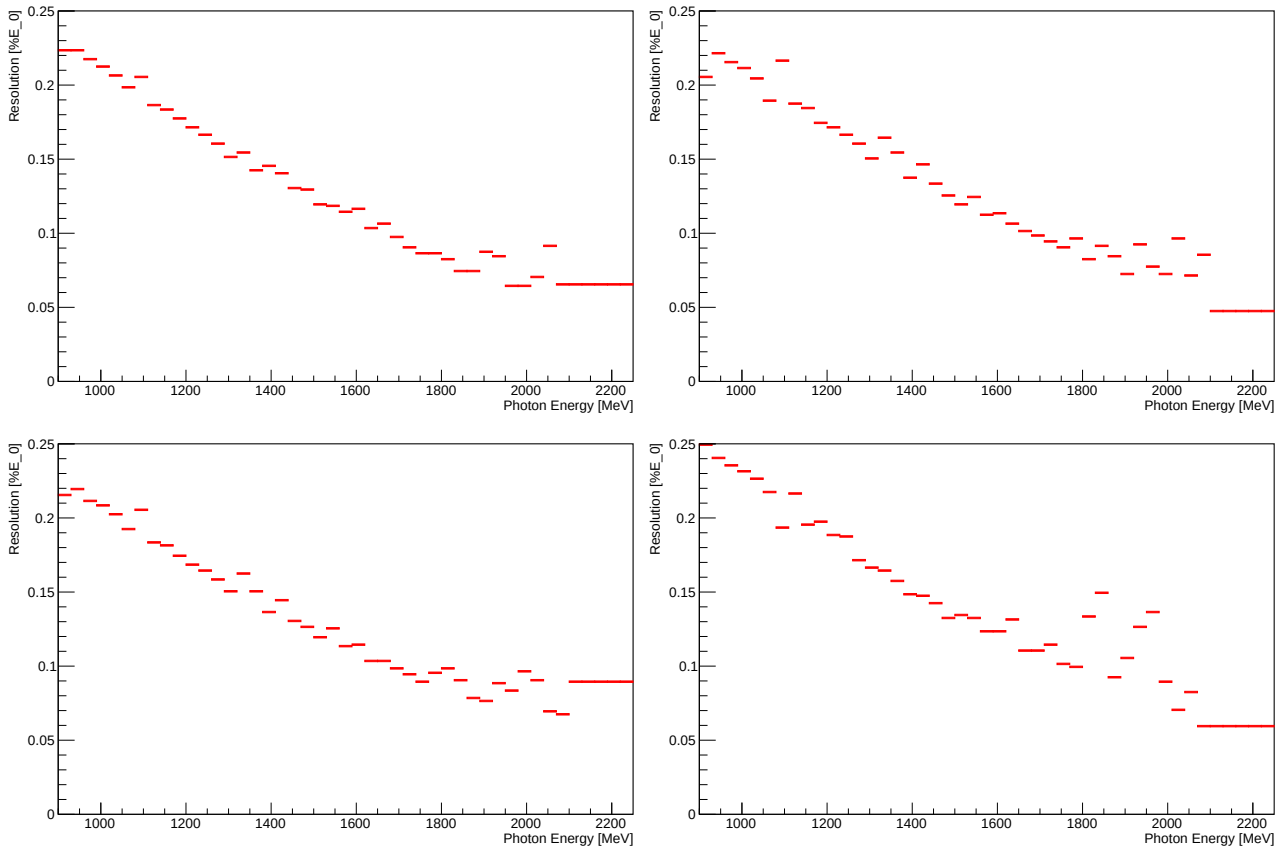

Figure 5.5: Energy resolution obtained in simulations for 0° (top left), 10° (top right), 20° (bottom left) and 10° with gaps (bottom right) for 3 layers of fibers.

5.2 Hardware components

Before presenting the prototypes and the final design a short overview of the used hardware (fibers, photomultiplier, FPGA and mezzanine read-out) should be given. The properties of the several hardware parts along some physical background will be presented.

5.2.1 Plastic scintillating fibers

Scintillators come in various ways such as organic or inorganic crystals, gaseous scintillators or plastic scintillators in their various forms. All of these share the common characteristic that they undergo luminescence after the material has been excited by ionizing particles. This means they re-emit the absorbed energy in the form of light. It is possible to delay this re-emitting process from nano-seconds to several hours in special materials.
Scintillation can be understood if one uses the simple picture shown in figure 5.6.

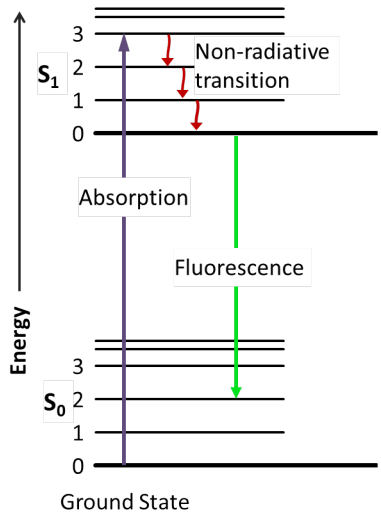

Figure 5.6: Simplified principle of fluorenscence.

The incoming ionizing particle excites an atom meaning that it moves to a higher energy level. Since this is an unstable situation the atom begins de-excitation. First, depending on the initially excited state, through photon free de-excitation, e.g. vibration (leading to a Stokes-shift), but at some point even through the emittion of a photon. As one can see the photon has a much lower energy than put in by the ionizing particle. This results in a higher wavelength of the emitted photon.
If the photon would have the complete deposited energy it could easily be re-absorbed. This would lead to a very low mean free path of the single photon so that only short fibers would give rise to a meaningful signal. To decrease this effect furthermore, additional wavelength shifters are used. These are materials that are doped into the scintillating material. They absorb a photon and re-emit it at a specific wavelength, which very unlikely will be re-absorbed by the scintillating material.

The term "plastic scintillator" typically refers to a scintillating material in which the primary fluorescent emitter is suspended in a solid polymer matrix. While this combination is typically accomplished through the dissolution of the fluorescent emitter prior to bulk polymerization, the emitter is sometimes associated with the polymer directly, either covalently or through coordination. The advantages of plastic scintillators include fairly high light output and a relatively quick signal, with a decay time of 2 - 4 nanoseconds. Another very big advantage of plastic scintillators is their ability to be shaped easily into almost any desired form which often allows a high degree of durability. [Wiki1]

For ARGUS the round fibers named "BCF-10" with double cladding from the company Saint Gobain[SGo2]

with 2mm diameter were used. The properties can be found in the data sheet on [SGo2]. For our purposes, on one hand, it was important that a high amount of ≈ 8000 photos would be produced for 1MeV of deposited energy so that enough photons reach the photomultiplier. On the other hand the doubled cladding should increase the amount of photons kept inside the fiber. Fibers are clad with two layers of material having a lower index of refraction. Due to this change in index of refraction, additional total reflection can be achieved at the surface and the photons will be kept inside the fiber. The trapping efficiency for the fibers used for ARGUS is about 3.4% for photons produced at the fiber axis up to $\approx 7\%$ for events near the cladding.
To perform correct simulations the minimal energy needed to be deposited in the fiber to produce a signal in the PMT that could be distinguished by 3σ from background needs to be calculated. As written before ≈ 8000 photons are produced for 1 MeV deposited in the scintillator. Since the electrons produced from ELSA are minimum-ionizing particles that follow

$$\Delta E\left(x\right) = 2\frac{\mathrm{MeVcm}^2}{\mathrm{g}} \cdot x \cdot \rho \tag{5.1}$$

with x the distance traversed in the material and ρ the density of the material. From [SGo2] it follows that $\rho = 1.05\frac{\mathrm{g}}{\mathrm{cm}^3}$. This leads for these fibers with 2mm diameter to $N\left(x\right) = \Delta E \cdot n = 16800\frac{\mathrm{x}}{\mathrm{cm}}$. With the given trapping efficiency of 3.4% this reduces to $N'\left(x\right) = N\left(x\right) \cdot \epsilon = 571\frac{\mathrm{x}}{\mathrm{cm}}$. Since the fibers are readout by the PMTs also their quantum efficiency must be taken into account. This leads to a final number of photons that are detected of $N^{''}\left(x\right) = N'\left(x\right) \cdot \epsilon_{qe} = 114\frac{\mathrm{x}}{\mathrm{cm}}$. This amount of photons should then be different by $3\sigma = 3\sqrt{N''} = 3\sqrt{114}$ from background. In the end this leads to a value for the minimum traveled distance in the scintillator of $x > 0.081$cm. This could again be given as an energy by using equation 5.1:

$$\Delta E_{min} = 170.1\mathrm{keV} \tag{5.2}$$

Since for ARGUS 16-channel-PMTs are used, as presented in the next part, it was clear that the fibers must be bent in some way to go from 3 layers to the 4x4 ordered PMT anodes. To make sure that this bending would not cause a significant loss of photons transported from one side to the other, tests were performed. The setup can be seen in figure 5.7.

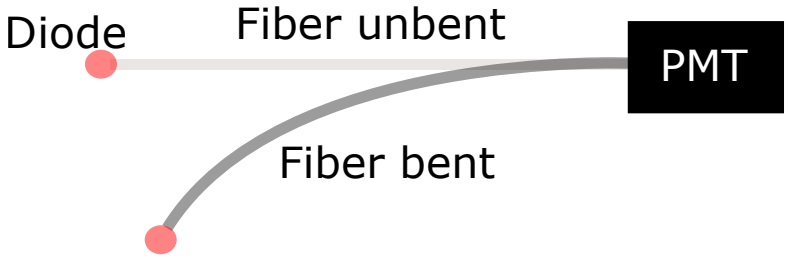

Figure 5.7: Schematic setup for fiber bending test.

One fiber is on one side coupled to the PMT and on the other side to a LED. Now for several bending radii and constant illumination through the LED, the signal height in the PMT was measured. The results are presented in table 5.1. As one can see the bending up to a bending radius of 40cm does affect the light output by only 1%. Measurements performed with heavy s-shaped bent fibers lead to a loss of 10%. Since this is far more than what is expected to be needed for ARGUS, the effect of bending could be neglected. The effect of producing cracks inside the scintillating material was visible as well during the tests under extreme circumstances.

bending radius r[cm]	signal s[mV]
"inf"	10.2
136 ± 13	10.1
64 ± 3	10.2
47 ± 2	10.2
40 ± 1	10.1

Table 5.1: Results of the bending test.

5.2.2 Multianode photomultiplier tubes

For the use as detectors, scintillators need to be read out via photomultipliers. A schematic view of a photomultiplier tube in general is shown in figure 5.8.

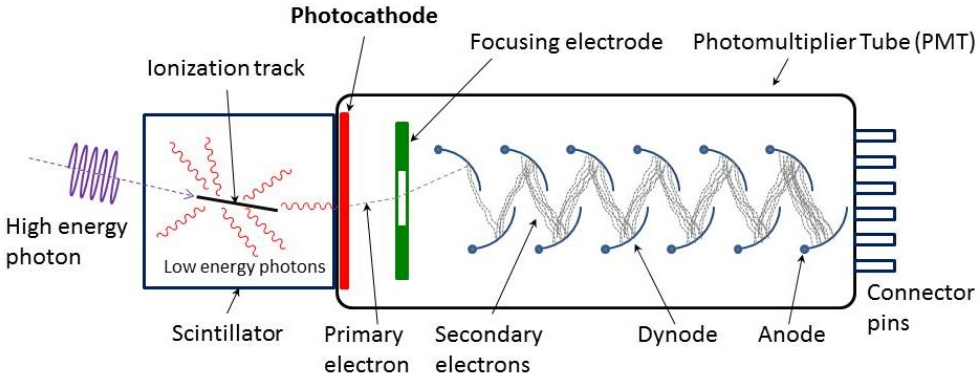

Figure 5.8: Working principle of a photomultiplier tube. For detailed description see text. From [Wiki2].

The low energetic photons from the scintillator hit the photocathode, a thin negatively charged layer, of the PMT and produce a free electron by the photoelectric effect. This primary electron is then focused on the first dynode. A dynode is an electrode in a vacuum tube that serves as an electron multiplier through secondary emission. To achieve this, the dynode is positive charged so that the primary electron is accelerated and gets enough energy to liberate more electrons. Since the second dynode is charged positive against the first dynode these electrons again produce new ones. This occurs several times until the 10^5 to 10^7 (depending on the amount of dynodes) in this way produced electrons hit the anode and produce a well measurable and sharp current pulse. Since all these dynodes need a potential difference to each other working voltages of several 100V are necessary.

For ARGUS the PMTs named H6568 [Ham1] by Hamamatsu [Ham2] are used. These are 16-channel photomultipliers. That means that 16 anodes are next to each other in one module and therefore the whole setup needs less space. Figure 5.10 shows a front view picture of such a PMT. These PMTs were chosen due to several points:

- to be able to detect the emitted wavelength of the scintillating plastic fibers (maximum of PMT at 420nm, fiber emitts at 432nm)
- the short anode response time of 0.83ns
- the low cross-talk between the channels of less than 1%
- high rate stability.

The anode rise time is the time between the production of the primary electron and the maximum of the anode current. Cross talk means the possibility that a signal on one anode produces a signal on the neighboring one. A test was performed to check the validity of the number given for the cross-talk. The setup can be seen in figure 5.9.

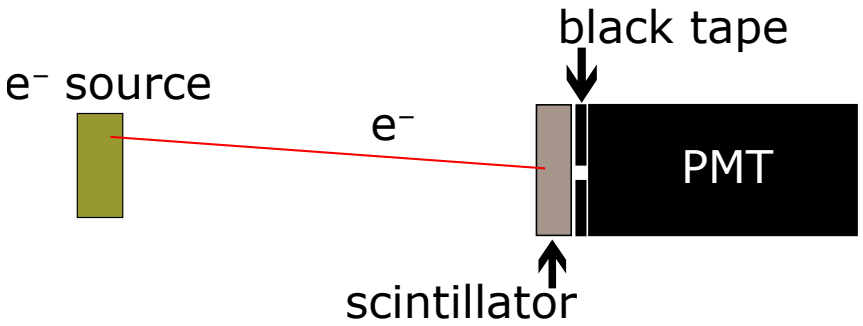

Figure 5.9: Schematic setup for cross talk measurement.

A radioactive source was used to produce photons in a piece of scintillating plastic in front of the multianode PMT which then could be detected by only one channel of the PMT. For this purpose the other channels were covered by black tape. Table 5.2 shows the results if only channel 11 could be reached by the photons.

P1	0	P5	0	P9	0	P13	0
P2	0	P6	0	P10	0	P14	0
P3	0	P7	1	P11	690	P15	1
P4	0	P8	0	P12	0	P16	1

Table 5.2: Result for Pixel 11 not covered with tape.

P1,P2 and so on denote the position of the pixel counting from the top left to the bottom right. As one can see the number of 1% given in the data sheet is valid for this channel and also for the others (see appendix A). Pixel 11 of the used PMT had some noise problems too since it produces a signal most of the times even if its not the open pixel or adjacent to another.

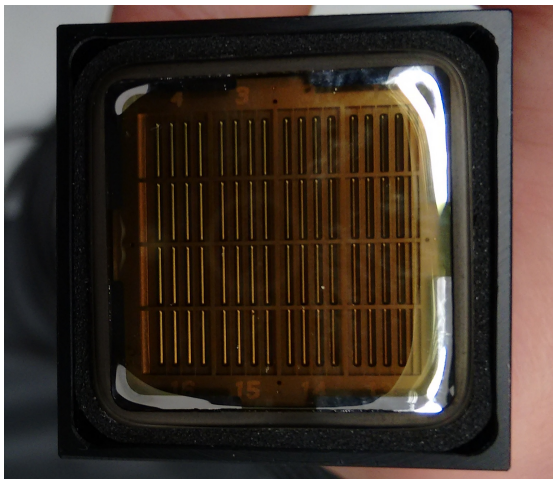

Figure 5.10: Picture of 16-channel PMT H6568 [Ham1] by Hamatsu.

5.2.3 FPGA and mezzanin read-out

The readout of the PMTs is done by the time over threshold (ToT) discriminator mezzanines on field programmable gate arrays (FPGAs).
Field programmable gate arrays are integrated circuits that can be programmed in various ways. This could be simple circuits such as a clock and can range up to complex circuits like microprocessors. After the program is loaded in the frame it is easily possible to change this circuit if something does not fit the expectations. This flexible behavior is one reason why these modules are use for several detectors in the BGO-OD experiment.

For ARGUS Spartan 6 boards by Xilinx are used. The firmware for the used FPGA is an in house development done by John Bieling called "jTDC". It allows to use the FPGA as TDC ("j" for credits to John Bieling). The PMT cables are therefore connected to a 16-channel ToT discriminator mezzanine. 3 of these mezzanines can be put on one FPGA board. For each channel a separate threshold (-4V to $+4$V) and hysteresis (0mV to 80mV) can be set.
Figure 5.11 illustrates the meaning of time over threshold, threshold and hysteresis.

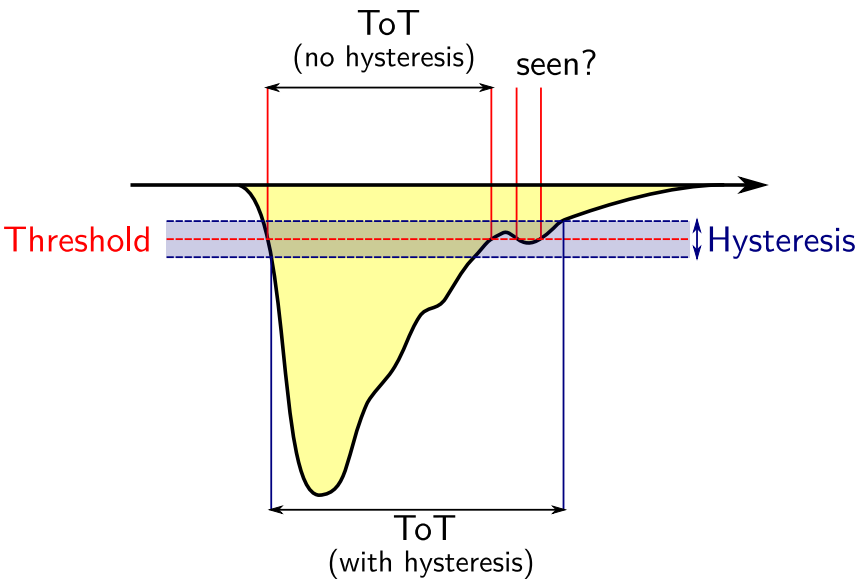

Figure 5.11: Definition of threshold, hysteresis and Time over Threshold (ToT). For detailed description see text. Figure from [FR15]

Time over threshold is the amount of time between the two points where the signal raise above the threshold and the point where it goes below the threshold. Thresholds are used to predict small noise signals to produce an output signal after the discriminator. In some cases, especially for the PMTs used for ARGUS, the analogue signal is not smooth. It can e.g. have smaller secondary peaks after the main peak. If the signal height would drop below the threshold between the two peaks, an additional ToT signal will be produced. To suppress these false signals one needs to lower the threshold or, since this could produce more noise, use a hysteresis. The hysteresis increases the upper threshold and decreases the lower threshold by the same adjustable amount. Therefore the second signal vanished on cost of a slightly longer ToT for the main signal.

5.3 First prototype

The hardware components in the previous section were used to set up a first prototype to test the usability of the planned geometrical design and should support the results gathered by the simulations presented in chapter 5.1. The design and test together with the results will be presented in this chapter.

5.3.1 Design

The results from chapter 5.1, clearly demonstrate that the three layer setup is the preferred design. Since one PMT can readout 16 fibers the decision to produce modules of 3 times 16 fibers ordered in the 3 layers, so 1 PMT for each layer, was made. This leads to the fact that on one side of the module there is 1 PMT while on the other one are 2. Figure 5.12 shows a 3D view of the needed aluminum and PVC parts as they were created using Autodesk Inventor 2009 [AI]. In the middle part also the fibers are visible as simple tubes.

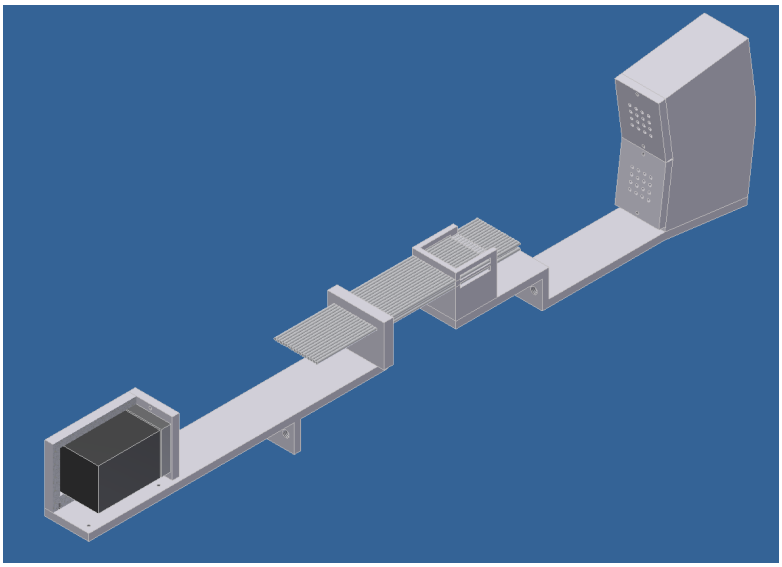

Figure 5.12: Inventor Studio picture of first ARGUS prototype.

The fibers generally are glued into 16 2mm holes ordered in a 4 x 4 matrix of a PVC part similar to the aluminum cap visible in 5.13 on the left. The PVC should prevent the fibers from scratches during the process of putting the fibers trough the holes. Each hole correspond to the position of one pixel on the PMT.
On the bottom left the single PMT housing is visible. A closer look on the housing can be seen in figure 5.13.

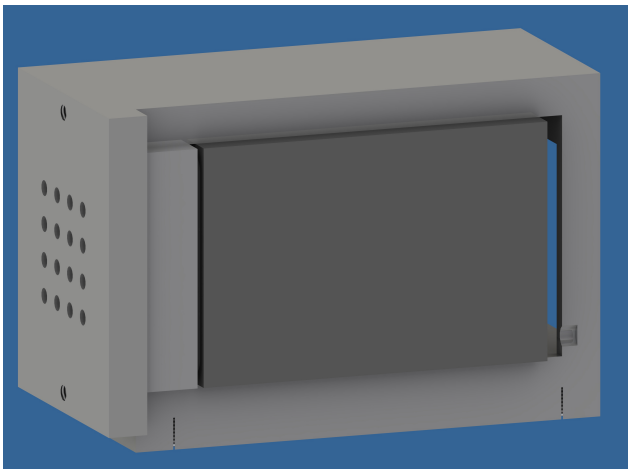

Figure 5.13: Profile of the first prototype PMT housing. Visible is the PMT itself inside the housing, the PVC fiber holder, the aluminium cap and also the holes for the springs can be seen.

The PMT together with the PVC fiber holding structure is inserted in the PMT housing from the inner side of the module. It is held in position by an aluminum lid which is screwed on the housing from the same side. On the back, inside the housing, springs press the PMT against the PVC fiber holder for best light coupling. The PMT cables will be guided through the large hole on the back. The housing for the two PMTs on the other side is very similar. In difference it is made of one part containing the two housings. To avoid different bending radii for the fibers on this side, the two PMTs are not parallel to each other.
The very important parts of the whole module are the two fiber holding structures in the middle. They are designed in a way to allow a positioning of the fibers to be closely packed. They must be different since on one side 2 layers entering the central region but on the other only one. The fibers of one side should go through the nearest part and go $\approx$ 1mm inside the material of the other side. Therefore the fibers should be fixed at their position. For each layer 16 holes with diameters of 2.1mm and 2.2mm are drilled. The latter for the planned usage with painted fibers. The gap between the two fiber holding structures is then the region where the beam passes. It is approximately 5cm wide to pretend interaction of the beam halo with the structure.

All parts were screwed together and mounted onto two rails that are connected with the tagger. The whole ARGUS module was then covered in black foil and tape to make it light tight. The position of the complete ARGUS module inside the tagging system can be seen in the Inventor Studios picture in 5.14 left side and the real picture in figure 5.14 on the right.

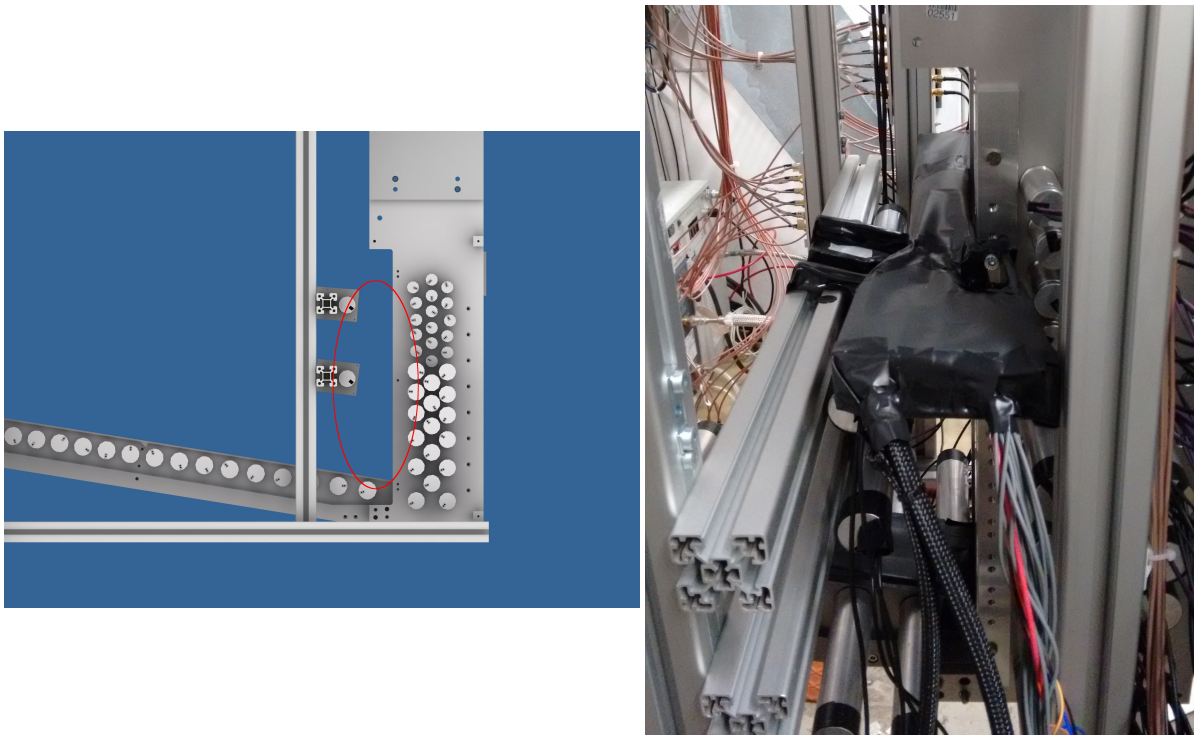

Figure 5.14: Positioning of ARGUS prototyp inside the tagging system shown using Inventor Studios (left) and for the real setup during the beamtime (right).

5.3.2 Tests and results

The first problem showed up during the assembling of the several parts presented above. It turned out, that painted fibers do not fit the 2.2mm holes in the different parts. It was not possible to put the fibers through the holes without producing scratches and an enormous amount of stress. Also the paint varied in thickness. Therefore it was decided to use the unpainted fibers with the 2.2mm setting of parts.

The main goals of the test beam time then performed in March 2015 were to understand the behavior of the read-out under real beam conditions and perform a test of the achievable efficiency.

To determine the efficiency an additional scintillating detector from an older thesis by Verena Muckhoff [Mu13] was used together with the Tagger. The setup can be seen in figure 5.15.

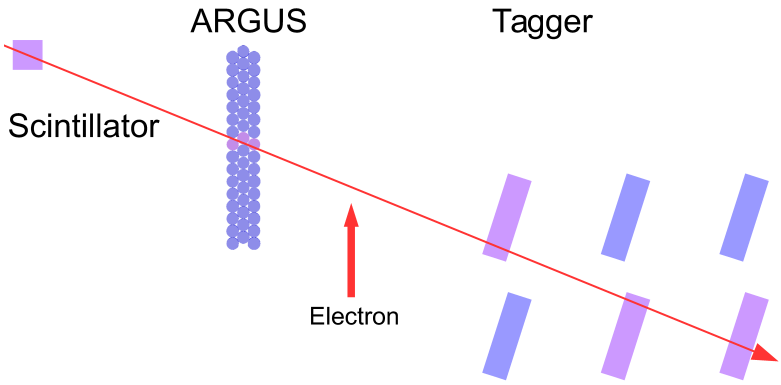

Figure 5.15: Schematic setup for efficiency measurement using a scintillating detector (left) and the current tagging system (right).

The scintillating detector was placed in front of ARGUS. Together with the tagger behind ARGUS it is possible to determine the efficiency trough:

$$\text{efficiency} = \frac{\#\text{ coincident electrons detected in ARGUS, Tagger and scintillator}}{\#\text{ coincident electrons detected in Tagger and scintillator}}. \tag{5.3}$$

To first order, effects such as multiple scattering, reduce the reliability of this kind of measurement. Therefore the efficiency is further on called "response" to make clear that there are other effects that have to be taken into account. The results for this test can be seen in figure 5.16.

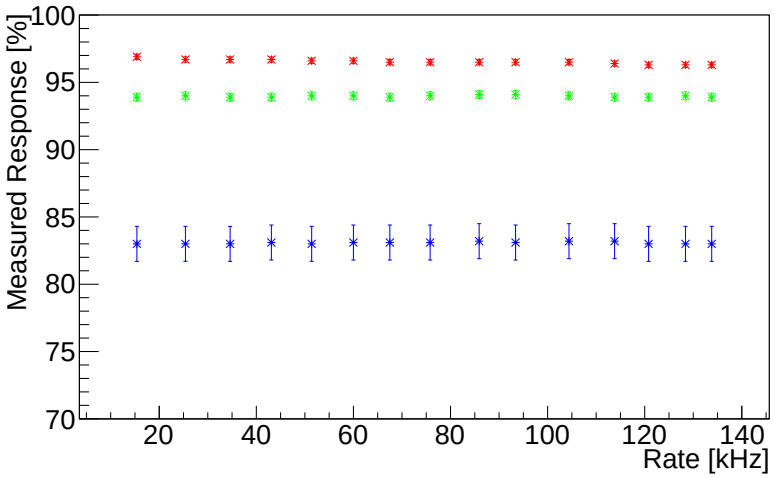

Figure 5.16: Results of efficiency measurement for three different types of measured response. Single hit response (red), intrinsic response (green) and multihit response (blue). For details see text.

Since the efficiency detector is smaller than the ARGUS module a central position was used to evade edge effects. The results show that the desired efficiency of about 99% cannot be confirmed if measured by this setup (blue datapoints in figure 5.16). Therefore other defined responses are investigated, too.
The "intrinsic response" (green datapoints in figure 5.16) is thereby given by the possibility that if ARGUS is hit by an electron and it produces a hit and the likelihood that it may produce a cluster. We call this the "clustering response". It is the most reliable quantity with a value of about 94%.
The single hit response (red datapoints in figure 5.16) only shows the possibility that ARGUS registered a single hit in time coincidence with the scintillating detector and the tagger. This efficiency is somewhat higher with 97% but also suffers from uncertainties like background.
Nonetheless, figure 5.16 also shows that, for each response, no dependence in detected rate for the measured rate values can be noticed. This is highly desired for the final detector.

In general, the results of this measurement have to be treated carefully. After the beam time it was visible that the fibers became loose at the position of the electron beam (figure 5.17). This could have happened when for rate tests, the module was moved to other positions on the tagger. Since it is not possible to distinguish when this happened, it could have spoiled the measurements for the efficiency/response. Also bad light coupling between the fibers and the PMTs could have an influence on this.

Figure 5.17: Loose fibers in the central region where the electrons hit ARGUS. Picture was taken after the test beamtime.

It was also tried to perform measurements of the coherent enhancement in the electron spectrum for linear polarization. Due to the width of the coherent edge which is larger than ARGUS and the loose fibers that were noticed at this point of the beamtime no reasonable data for this could be obtained.

To eliminate the error sources shown by this short beamtime, an improved version of the prototype was designed. It will be presented in the next chapter together with the obtained results.

5.4 Second prototype

5.4.1 Improved design

The second prototype design was invented using the knowledge and results achieved from the test with the first prototype. Figure 5.18 shows this new construction.

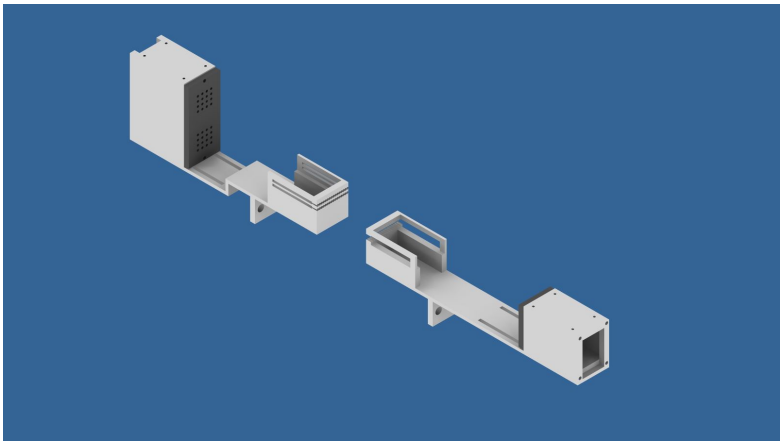

Figure 5.18: Inventor Studio overview of second ARGUS prototype.

The main changes were made to the PMT housing structures. Since the side plates are very thin the production of the whole object out of a complete aluminum block would take too long. For this reason, the PMT holding was separated in several parts as visible in figure 5.19.

Figure 5.19: PMT housing structures in its improved version.

The sides are made out of 0.5mm thin aluminum plates (brownish parts in 5.19). Top and bottom sides, and the middle on the 2 PMTs side, are made thicker to give some structural integrity (blue parts in 5.19). Furthermore, the 2 PMTs on the one side are now parallel to each other. To obtain similar bending radii for the fibers and to reduce the overall high of the detector, there is a step in the aluminum rail on which the PMT housings are mounted. The front cap is completely out of PVC and combining the function of the previous PVC 4x4 fiber holding part and the previous aluminum cap (see figure C.1 in the appendix). Therefore the fibers are not needed to be put through 2 holes on this side. Since in the previous design the PMT must be put inside the PMT housing from the fiber side this doesn't provide any possibility to be done in the final complete setup. Therefore the front plate with the fibers is screwed on there once. The back plate was changed to give the possibility to put in or exchange the PMT from this side (green parts in figure 5.19 or overview in figure 5.18). The springs are still positioned in holes drilled in this back plate. Through screwing the back plate to the top and bottom side, the PMT will be pressured slightly against the PVC fiber holder providing a good coupling.

The central fiber holding parts made of aluminum were changed too. The holes now have a diameter of 2.2mm to reduce scratches and reduce the stress on the fibers. The longer sides of these parts are also for decreasing the stress on the fibers. One major change was made to prevent the problem of falling apart of the fiber position structure of the first prototype. For this all fibers entering the central region from the 2 PMT side are now put through the others side holding structure by at least 2mm. This increases the structural integrity a lot. Figure 5.20 shows a picture of the module during construction (some parts are still missing). Figure 5.21 shows that the fibers are in the desired position (except, as expected, the edge fibers) when using this new design.

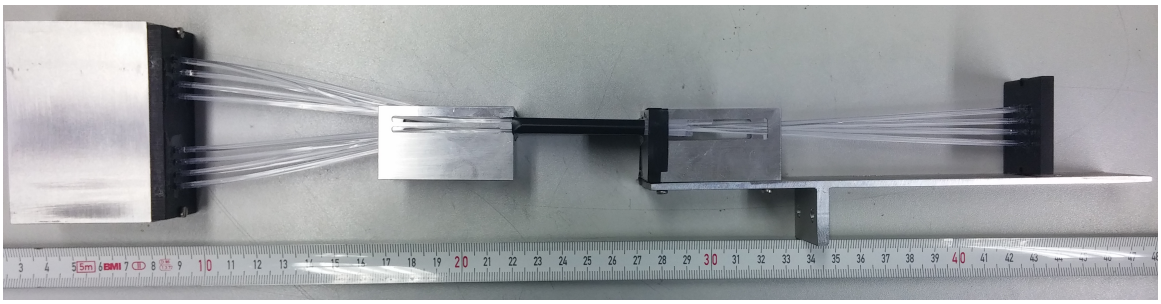

Figure 5.20: second ARGUS prototype during construction.

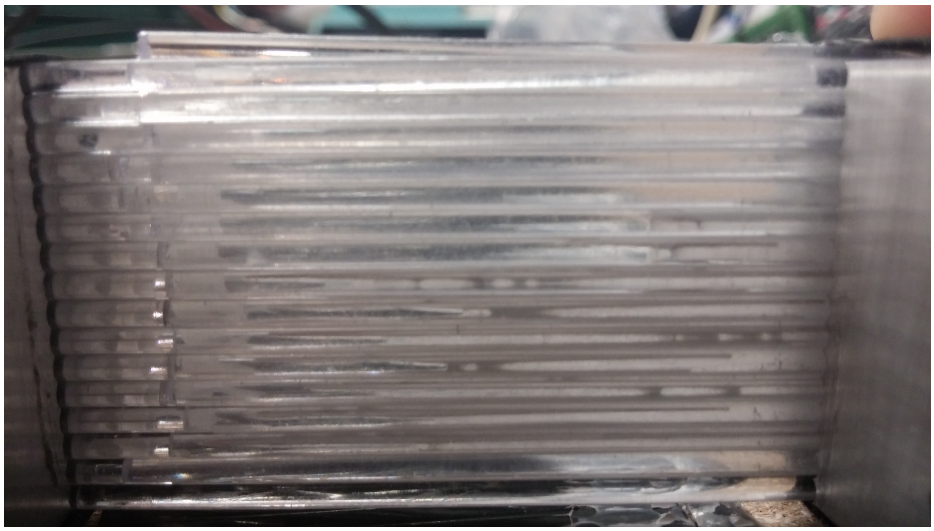

Figure 5.21: Picture of the 3 layers after assembling the second prototype.

5.4.2 Tests and results

As expected, assembling the parts was much easier than for the first prototype. So from this point no problems showed up. Again a short beam test in May 2015 was used to measure the response using the same setup as already presented in chapter 5.3.2.

This time a measured response in the multiple hit case, meaning getting a cluster consisting of minimum two hits, of about 95% could be obtained. This is a huge improvement to the 83% measured before.

Since this time the detector was build more stable and has this high "efficiency" the coherent edge in the electron spectrum was moved to the position of the ARGUS module and therefore could be measured by ARGUS. Since the edge is still broader than one ARGUS module it cannot be seen as a sharp edge. But as visible in figure 5.22 the coherent edge can be seen as it moves through the electron spectrum during a so called STONEHENGE RUN. During a STONEHENGE RUN the diamond radiator is moved in a cone around the electron beam position. This leads to changes in contributing lattice vectors as presented in chapter 3 and therefore changes in the total cross section. For each step in this cone an electron spectrum of ARGUS was taken. Figure 5.22 now shows the change in rate when the coherent edges (different high means different contributing lattice vectors) hit this channel. The double peak structure is expected and can be understood by having a look on the stonehenge plot in figure 5.23 where figure 5.22 represents a slice in this plot.

So even without the ability of measuring the coherent edge directly with only one module it was verified that ARGUS could do this as a full detector.

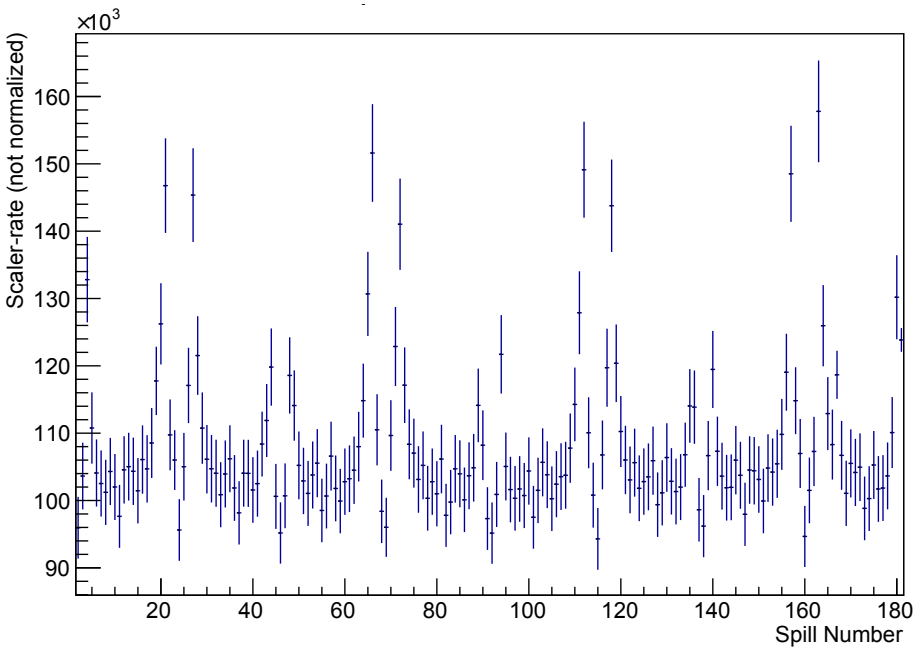

Figure 5.22: Rate in fiber 22 of the second prototype during a STONEHENGE RUN. Each peak of the same hight corresponds to the first or second coherent edge.

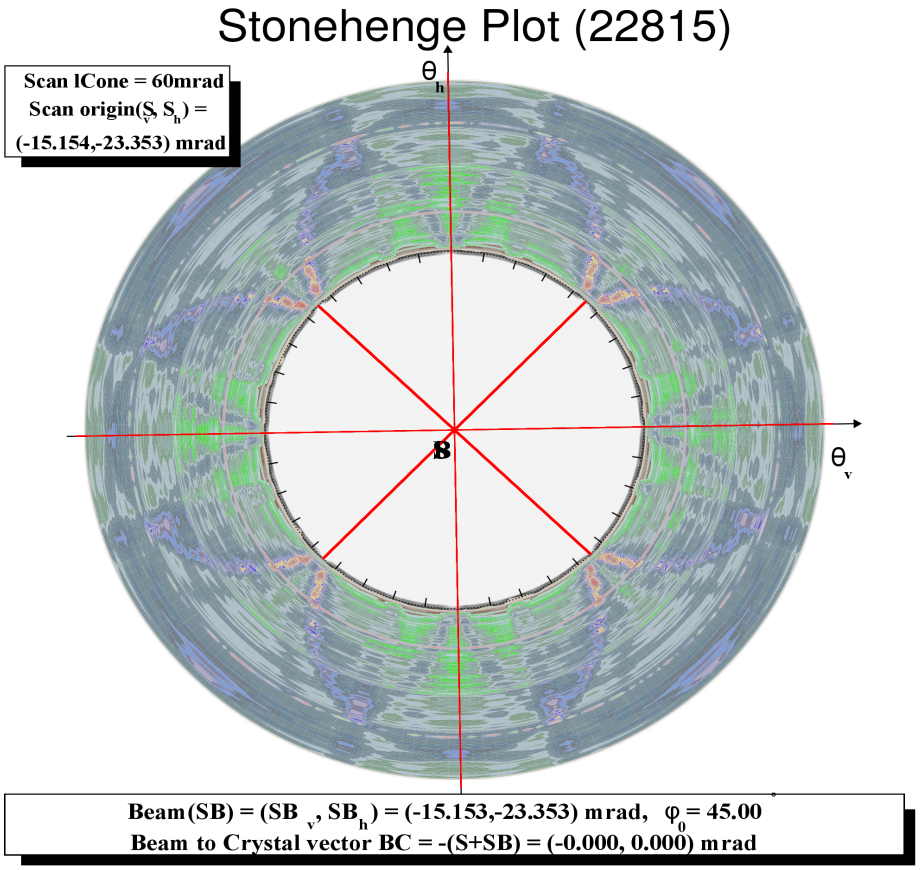

Figure 5.23: Stonehenge plot for an aligned crystal measured with the existing tagger. The photon energy rises towards the out, and therefore each slice corresponds to a tagger channel. The periodic and double peaked structure can be seen clearly.

5.5 Final setup

The final setup was constructed with all the knowledge from the previous tests. Furthermore it is the first time all available modules, only limited by the amount of PMTs and fibers, are put together to work as the desired complete detector. 10 complete modules were built, each making use of 3 PMTs and 48 fibers. Only small changes on the constructed aluminum parts were made. It was tried to reduce the overall height of the detector slightly further because the space between tagger and Moeller detector would not be sufficient for the previous design if expanded to the whole detector. Due to limited read out electronics only half of the ARGUS modules could be read out simultaneously. A look on the full detector during construction can be seen in figure 5.25 and more in appendix C.2.

The following measurements were performed during the 3 week beamtime in June 2015. This time a rough gain matching of all the used PMTs were performed to reduce the effect of different count rates due to different gains. For this figure 5.24 was used together with the final test sheet of the PMTs. The PMT with the lowest gain of $3.3 \cdot 10^6$ was set to be the normal gain. This PTMs voltage was set to the normal working voltage of 800V. With the relation between voltage and gain in figure 5.24 the voltage of all the other PMTs was set in respect to the 800V nominal PMT. The so obtained voltages together with the gains can be read in appendix B.

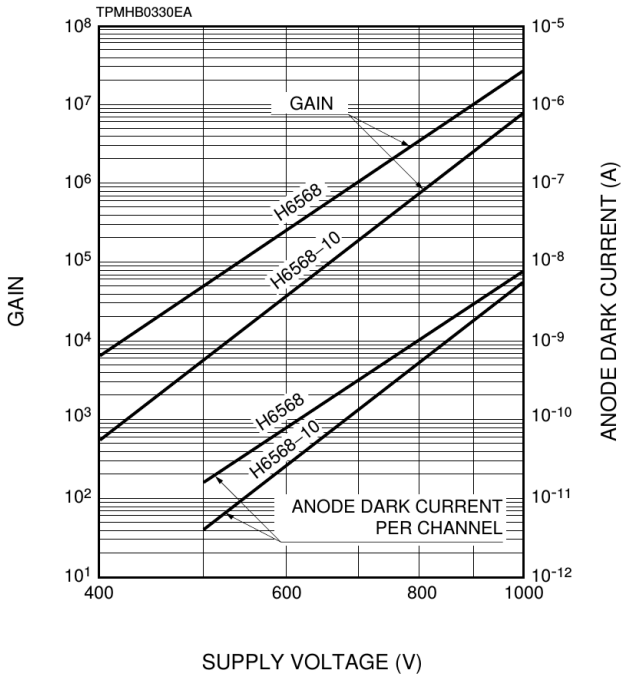

Figure 5.24: Relation between gain, dark current and supply voltage of the PMTs.

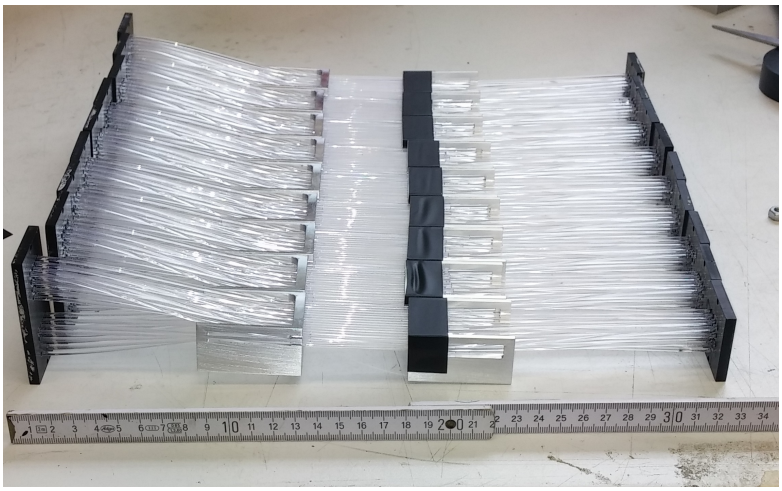

Figure 5.25: Picture of final detector during construction.

5.5.1 Energy calibration and efficiency

To make use of the electron energy information that ARGUS provides, an energy calibration is needed. As already mentioned in chapter 4 the electrons from ELSA are bent in the tagging magnet due to the Lorentz force $F_L = q \cdot v \cdot B$. Since the velocity can be expressed using the momentum and the electrons are relativistic, their momentum is equal to their energy. Thus resulting in $F_L \propto E \cdot B$. The magnetic field needed to bend an electron in a specific channel B_{ch} can therefore determined using

$$B_{\mathrm{ch}} = \frac{E_0}{E_{\mathrm{ch}}} \cdot B_0 \tag{5.4}$$

with E_0 the used ELSA energy for calibration, B_0 the corresponding nominal magnetic field value of the tagging magnet, E_{ch} the electron energy needed to hit this specific channel for B_0. Equation 5.4 can therefore

used to determine the relative energy of each channel

$$\frac{E_{\mathrm{ch}}}{E_0} = \frac{B_0}{B_{\mathrm{ch}}} \tag{5.5}$$

$$\tag{5.6}$$

by measuring the needed B_{ch} to hit this channel with the primary beam.
For the measurement a low intensity (0.05pA) primary electron beam (without any radiator in between) was swept over the detector. The low intensity is used to protect ARGUS from getting damaged by radiation and high count rate. The sweeping was performed by varying the field strength of the tagging magnet. This leads to a plot shown in figure 5.26 for every channel.

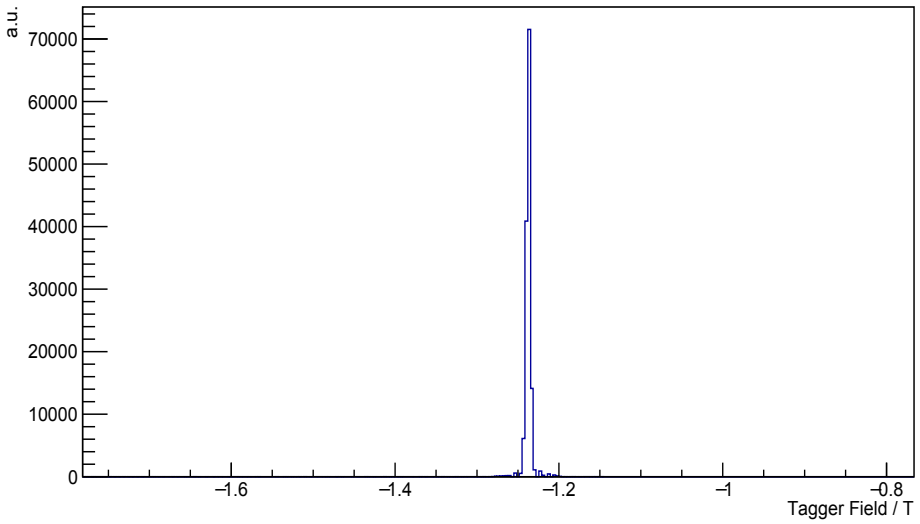

Figure 5.26: Hits in one channel of ARGUS as function of the tagging magnetic field.

Plotted is the number of hits in this channel as function of the magnetic field strength. By fitting a Gaussian distribution to these datapoints the needed field to bend the electron in this channel B_{ch} can be determined which than leads to E_{ch}. Since only half of the ARGUS detector could be read out, the calibration was done seperately for three overlapping parts. The results of this energy calibration can be seen in figure 5.27 for the full detector range.

Additionally, the energy width of each channel, and therefore nothing else than the energy resolution of ARGUS, can be determined too. It is calculated using

$$\frac{\Delta E_{\mathrm{ch}}}{E_{\mathrm{ch}}} = B_0 \left(\frac{1}{B_{\mathrm{ch}} - \Delta B_{\mathrm{ch}}} - \frac{1}{B_{\mathrm{ch}} + \Delta B_{\mathrm{ch}}} \right) \tag{5.7}$$

where ΔB_{ch} is the sigma of the fitted Gaussian in figure 5.26. Due to the minimum width of the beam of about 4mm which is larger than the fiber diameter, the calculation of the energy resolution should be treated carefully. The obtained values can be seen in figure 5.28.

The results obtained for the existing tagger were already presented in figure 4.2. If one compares this with the ARGUS plot one sees that the desired improvement of the resolution was achieved.

Again the efficiency was checked with the same method presented before for the prototype modules. An efficiency of 95% could be reached.

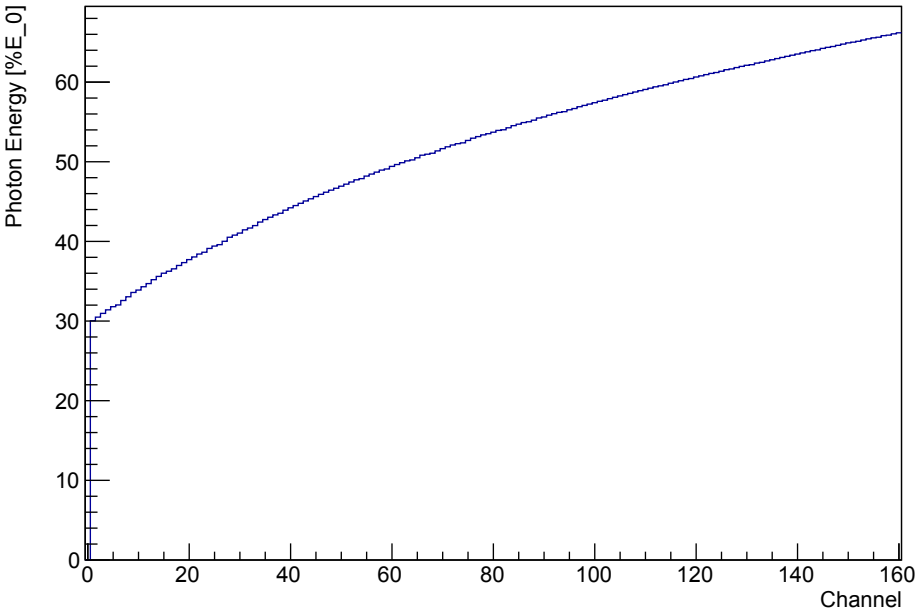

Figure 5.27: Energy calibration of ARGUS for the full detector range.

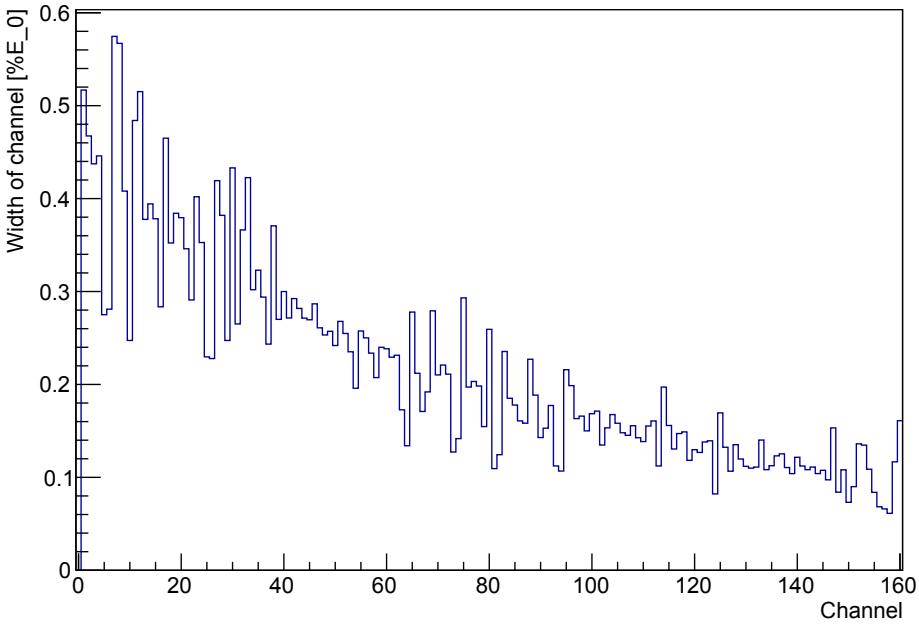

Figure 5.28: Energy resolution obtained for measurements with the final detector.

5.5.2 Measuring the coherent edge

This beamtime half of ARGUS could be read out and therefore a larger part of the photon spectrum could be measured. Especially the region with the main coherent peak should be covered with ARGUS even for further analyses. For this also the energy calibration was necessary. The photon spectrum obtained using the ARGUS modules in the region of the coherent edge can be seen in figure 5.29. For better visualibility the spectrum of a coherent run (diamond radiator) was divided by that of an incoherent (copper radiator with 100μm thickness) to decrease the incoherent contribution of the bremsstrahlung process. The main coherent enhancement is clearly noticeable. Figure 5.30 shows a comparison of the obtained divided photon spectrum for the tagger

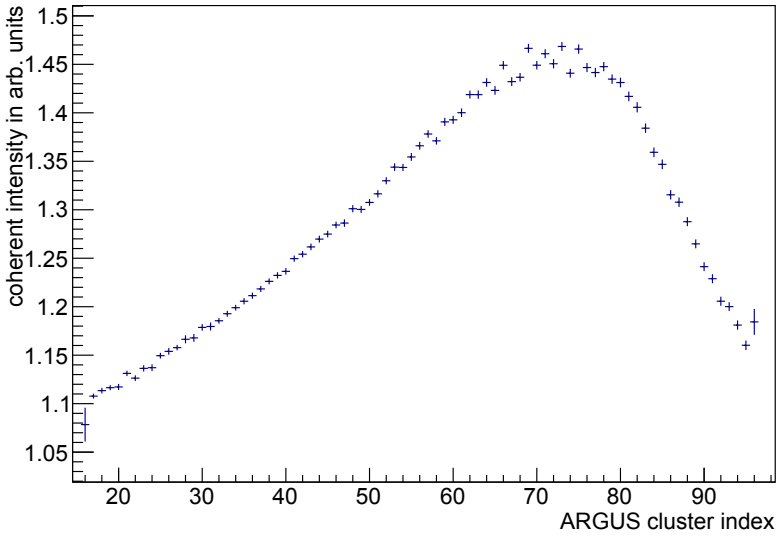

Figure 5.29: Relative ARGUS spectrum in the region of the first coherent enhancement.

and ARGUS and the calculations using COBRIS. The whole region could be covered by ARGUS due to two separate measurements with different active modules. The data of ARGUS fit well to the calculations. The deviation in the peak between the tagger datapoints and the calculation is due to rate instabilities of the tagger PMTs. ARGUS is not affected by this because the rate of one tagger channel is divided into several fibers leading to a lower rate per fiber.

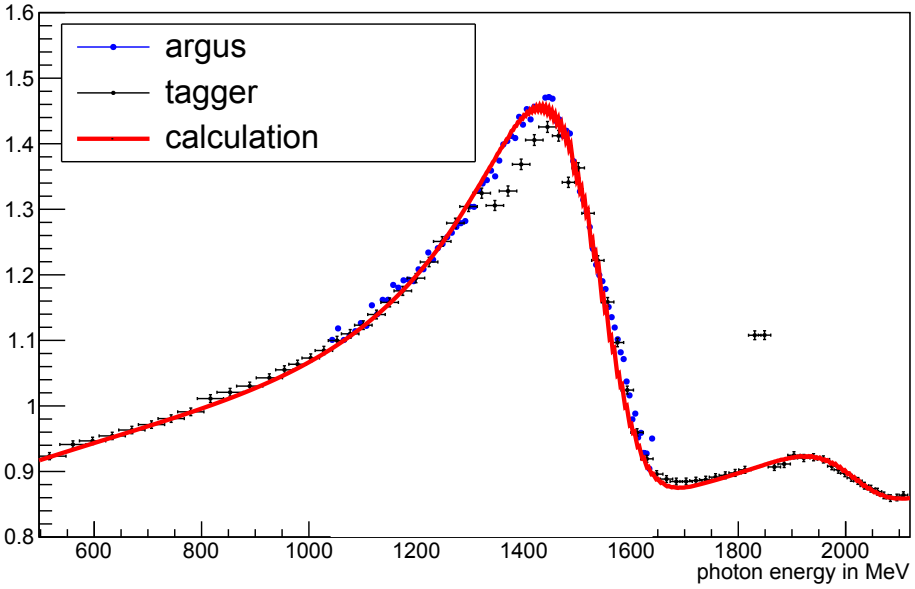

Figure 5.30: Relative ARGUS and tagger spectrum compared with simulation performed using COBRIS.

5.6 ARGUS - Summary and outlook

The setup of the scintillating fiber detector ARGUS was performed in 3 steps. First simulations showed that an improvement of the energy resolution is possible. To obtain a maximum of efficiency a design of 3 layers of scintillation fibers is preferred.
These results lead to the design of the first prototype. It was tested under real conditions inside the experiment hall. The results show a smaller efficiency than expected with a value of about 83% compared to the $> 99\%$ obtained from simulations. The results could be explained by the poor positioning of the fibers in the interaction region with the beam.
Based on our experience, we built a second prototype, which proved to be quite an improvement. Again measurements for the efficiency were performed that lead to values about 95% which is better then for the first prototype and, since it is constant over the whole detector, enough for the final construction. Data of the rate in one ARGUS fiber were taken for different positions of the coherent edge, leading to results that show, that ARGUS as a full detector will be able to measure the shape of the coherent edge.
The final setup of the detector consists of 10 modules very similar to the second prototype. They were put together and installed in the existing tagging system for a longer data taking period. As a first step, an energy calibration were performed whith results, that are consistent with the already existing tagger. Also the precise energy resolution was determined for the covered energy region. An overall improvement compared to the tagger could be validated. With the now larger operating part it was possible to measure the shape of the first coherent edge completely.

So all in all the ARGUS was setup successfully and is now an operating part of the experiment. The properties that could be determined all fit the expectations. Now the electronics need to be completed so that all modules of the complete ARGUS will be able to take data simultaneously. Then also a new energy calibration together with fine tuning in the gain matching and threshold adjustments will need to be performed. To summarize, we have an high-resolution detector for precisely finding the coherent peak.

6 Consistency check of the degree of polarization obtained from analytic bremsstrahlung calculations by investigating the beam asymmetry Σ in $\pi^0 p$ photoproduction

The impact of the better energy resolution of ARGUS on the systematical error of the determination of the degree of polarization should be investigated. The degree of polarization with its systematic error is determined using the COBRIS program from [Be]. To validate that this program works correct, the degree of polarization is also determined making use of the $\pi^0 p$ beam asymmetry.

This chapter should also give a short insight into the topic of polarization observables. Here, only the photoproduction of a pseudoscalar meson like the pion is taken into concern. In vectormeson photoproduction one more degree of freedom exists, leading to additional measurable observables. For a detailed description [PST96] can be studied.
First some general remarks on the kinematics and cross section will be given. Then more details to the, later in this chapter, investigated beam asymmetry Σ will be presented. The last part of this chapter is the reconstruction of the $\pi^0 p$ final state measured with the BGO-OD setup for investigating the beam asymmetry. With the measured asymmetry, a determination of the degree of polarization will be performed. These data will be compared with results obtained with the COBRIS program. The analysis and comparison will be performed separately with the already existing tagging system and the new ARGUS detector.

6.1 Polarization observables

6.1.1 Kinematics

In photoproduction of mesons two variables are enough to describe the complete kinematics. In most cases the photon energy E_γ together with the polar angle of the meson in the center of mass system[8] Θ_{CMS} are used. For photoproduction of pseudo scalar mesons (e.g. π^0) the incoming photon, the target proton or recoil proton can be polarized. The linear polarization of the photon beam can be denoted with $P_{\gamma,l}$ and the right handed circular polarization with $P_{\gamma,\odot}$. For the target and recoil proton polarization the vectors $\vec{P}^T = \left(P_x^T, P_y^T, P_z^T\right)$ and $\vec{P}^R = \left(P_x^R, P_y^R, P_z^R\right)$ are needed.

6.1.2 Cross section

The expression for the differential cross section depends on which type of polarization is used in the experiment [KDT95]:

- polarized photons and polarized target:

$$\begin{aligned}\frac{d\sigma}{d\Omega} &= \frac{d\sigma_0}{d\Omega}[1 - P_{\gamma,l}\Sigma\cos 2\phi \\ &+ P_x^T\left(-P_{\gamma,l}H\sin 2\phi + P_{\gamma,\odot}F\right) \\ &- P_y^T\left(-T + P_{\gamma,l}P\cos 2\phi\right) \\ &- P_z^T\left(-P_{\gamma,l}G\sin 2\phi + P_{\gamma,\odot}E\right)]\end{aligned} \tag{6.1}$$

- polarized photons and recoil polarization:

$$\begin{aligned}\frac{d\sigma}{d\Omega} &= \frac{d\sigma_0}{d\Omega}[1 - P_{\gamma,l}\Sigma\cos 2\phi \\ &+ P_x^R\left(-P_{\gamma,l}O_x\sin 2\phi + P_{\gamma,\odot}C_x\right) \\ &- P_y^R\left(-P + P_{\gamma,l}T\cos 2\phi\right) \\ &- P_z^R\left(-P_{\gamma,l}O_x\sin 2\phi + P_{\gamma,\odot}C_x\right)]\end{aligned} \tag{6.2}$$

[8] short:CMS

- polarized target and recoil polarization:

$$\begin{aligned}\frac{d\sigma}{d\Omega} &= \frac{d\sigma_0}{d\Omega}[1 + P_y^R P \\ &+ P_x^T \left(P_x^R T_x + P_z^R T_z\right) \\ &+ P_y^T \left(T + P_y^R \Sigma\right) \\ &- P_z^T \left(P_x^R L_x - P_z^R L_x\right)] \end{aligned} \tag{6.3}$$

The angle ϕ hereby denotes the azimuthal angle between the polarization vector of the photon and the reaction plane as can be seen in figure 6.1 and σ_0 denotes the unpolarized differential cross section.

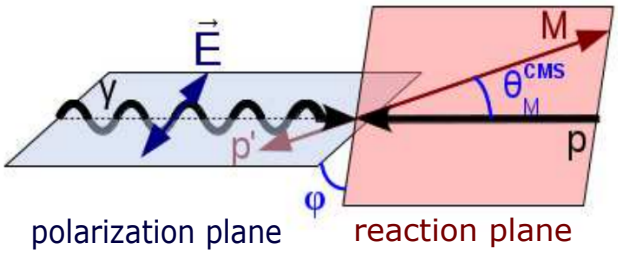

Figure 6.1: Definition of angles between polarization and reaction plane in CMS. The reaction plane is given by the target proton (p) and the meson (M) directions. From [EB12].

So in total for the meson photoproduction case one ends up with the polarization observables shown in table 6.1. In this table each polarization oversable appears two times meaning that it could be measured using two different experimental setups. For performing a "complete measurement" of the photoproduction cross section 8 out of these 16 observables are needed [CHT97]. In any case the unpolarized cross section σ_0 beside the three single polarization observables (Σ,T,P) needs to be measured. All possible combinations given by pure mathematical consideration are listed in [CHT97]. However, due to limitations in experimental accuracy, more than these 8 observables need to be measured [SHKL11].

photon		target			recoil			target+recoil			
	-	-	-	-	x'	y'	z'	x'	x'	z'	z'
	-	x	y	z	-	-	-	x	z	x	z
unpol. (T)	σ_0	0	T	0	0	P	0	$T_{x'}$	$-L_{x'}$	$T_{x'}$	$L_{x'}$
linear pol. (TT)	$-\Sigma$	H	$(-P)$	$-G$	$O_{x'}$	$(-T)$	$O_{x'}$	$(-L_{x'})$	$(T_{x'})$	$(-L_{x'})$	$(-T_{x'})$
circular pol. (TT')	0	F	0	$-E$	$-C_{x'}$	0	$-C_{x'}$	0	0	0	0

Table 6.1: polarization observables in meson photoproduction. The entries in brackets denote polarization observables, which also appear elsewhere in the table.[KDT95]

6.1.3 The beam asymmetry Σ

As shown in equation 6.1 the beam asymmetry Σ has a $\cos(2\phi)$ dependency. An explanation of the occurrence of this can be found in [SCH09].
The reason for this asymmetry can be explained by coupling between the spin of the baryon ($\vec{S}$) and the orbital momentum of the baryon and meson in the final state ($\vec{L}$). The effective potential can then be described as $V = V_0 + V_{LS}\vec{L}\vec{S}$. This additional potential favored a parallel or anti-parallel orientation of spin and orbital momentum. For an unpolarized photon beam and target, this potential is symmetric (figure 6.2 on the left).

For linear polarized photons however this situation changes. Let assume that the photon is polarized in x-direction. Due to the favored orientation of the polarization, one gets beside the electric field in this direction an additional magnetic field in y-direction. The characteristic $\cos(2\phi)$ dependency can be achieved either through coupling of the electric or the magnetic field of the photon to the target proton. In case of an electric coupling the beam asymmetry is always negative. This is due to a charge separation of the electric field of the

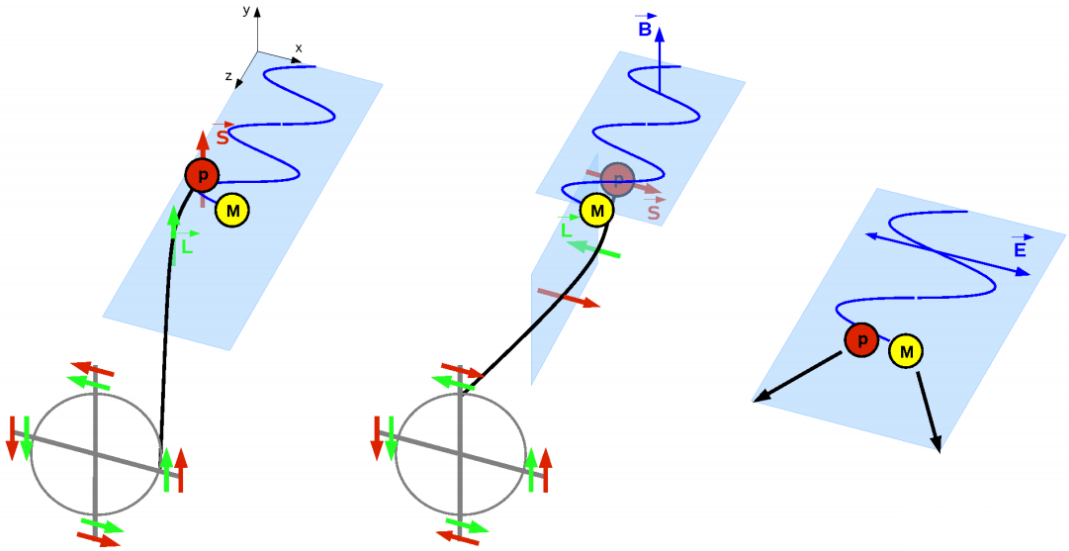

Figure 6.2: Schematic explanation of the beam asymmetry's occurrence: On the left: Both, photon and target proton are unpolarized. The resulting distribution is azimuthal symmetric. Middle: Meson photoproduction with linear polarized photons. Through the magnetic field, the spin of the target particle is flipped leading to a $\cos(2\phi)$ asymmetry. Right: the electric field of the photon leads to a charge separation and therefore a $\cos(2\phi)$ asymmetry. From [EB12]

photon (figure 6.2 on the right).
For an magnetic coupling to the target proton the proton spin can be flipped. This is possible via precession if the proton spin has a component orthogonal to the magnetic field direction of the incoming photon. Baryons with a spin parallel to the magnetic field are not affected by this. Together with the potential mentioned above, this leads to the characteristic $\cos(2\phi)$ dependency (figure 6.2 middle). For magnetic coupling the beam asymmetry can be either positive or negative, depending on the potential of the coupling.

6.2 Reconstruction of the $\pi^0 p$ final state

Events are selected according to the "participant-spectator" scheme. It assumes that the incoming photon interacts only with the "participant" nucleon, whereas the other acts as a "spectator". Processes are then treated as two-body reactions, if the target nucleon was free. Events will then be classified according to the reaction

$$\gamma p\,(n) \rightarrow \pi^0 p\,(n) \rightarrow \gamma\gamma p\,(n)\,.$$

The π^0 is reconstructed through its decay in 2 photons detected by the central detector of the BGO-OD experiment.
Photons that are produced in the central part are only detected by the BGO ball. Photons produce large clusters due to a broad shower produced in the mainly hit crystal. If for one photon event in the tagger, two photons in the BGO are produced these are suggested to be a meson and therefore their four-vectors are summed up.

The proton can be detected either in the central detector, in the new scintillating ring detector (SciRi) [SCHE15] or in the forward spectrometer. For this thesis only BGO and SciRi are used. The statistic in the forward spectrometer is not very high, so leaving these events out does not change systematic errors much. Inside the BGO ball protons produce small clusters and additionally, due to their charge, a signal in the scintillating barrel. Due to this, protons can be distinguished well from photons in the central part.

With the kinematical cuts:

- time cuts between the different particles involved
- cut on $E_{\gamma,measured} - E_{\gamma,calc}$ of the tagger photon
- selecting the best fitting photon and proton
- cut on angle difference between proton candidate and missing particle
- cut on the π^0-mass
- coplanarity cut between π^0 and proton
- cut on $E_{\pi^0,measured} - E_{\pi^0,calc}$
- missing mass cut

presented in detail in the next chapters, the event selection is cleaned up to make sure that the selected events are real $\pi^0 p$ events. Each time a Gaussian distribution is fitted, 3σ of the events are chosen for the further analysis. The analysis was performed twice, for electrons detected only by the existing tagging system and electrons only detected with ARGUS.

6.2.1 Time cuts

The first set of cuts is performed to make sure that the detected particles in the central detector and the incident photon detected in the tagger are in time coincidence with each other for each event. To do so, first the time difference between tagger or ARGUS electron and the two BGO photons is plotted as shown in figure 6.3.
The same was done for the difference between the two photons inside the BGO. The distribution with fit is shown in figure 6.4, leading to $\sigma = 1.53$ns. Also the time difference between the proton inside the BGO and the tagger electron was investigated leading to the plot in figure 6.5. Data obtained with the tagger on the left and with ARGUS on the right.

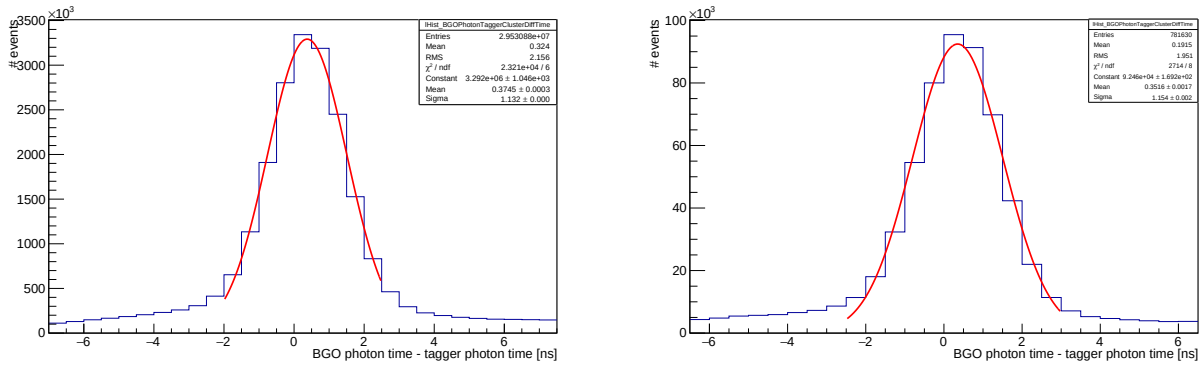

Figure 6.3: Time difference tagged photon - BGO photons, making use of the existing tagging system (left) or ARGUS (right).

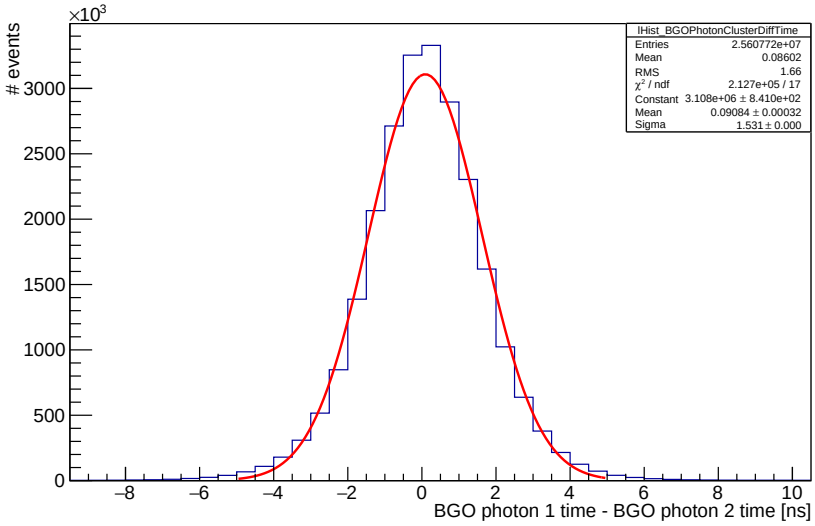

Figure 6.4: Time difference between both BGO photons.

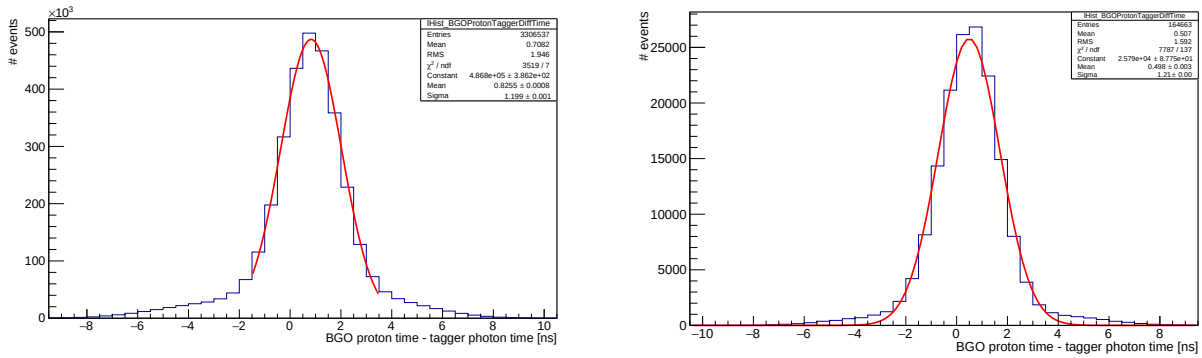

Figure 6.5: Time difference tagged photon - BGO protons, making use of the existing tagging system (left) or ARGUS (right).

6.2.2 Selecting the best fitting tagger electron

In one trigger event it is possible, that the tagger registered two or more electrons. Therefore the right photon energy which leads to the π^0 productions is not known. To solve this ambiguity, first the reconstructed meson was used to calculate the expected tagger energy using

$$E_{\gamma,\mathrm{calc}} = \frac{m_p E_{\mathrm{meson}} + \frac{1}{2}\left(E^2_{\mathrm{meson}} - \vec{p}^{\,2}_{\mathrm{meson}}\right)}{m_p - E_{\mathrm{meson}} + p_{\mathrm{meson,z}}}. \tag{6.4}$$

The dependence between calculated and measured photon energy in the tagger is shown in figure 6.6 for both the tagger and ARGUS. Beneath the diagonal band corresponding to valid events, also some background especially in the upper left is visible. This mainly comes from hadronic events taking place inside the BGO which had no corresponding electron detected in the tagging system. By using a cut on the diagonal where calculated and measured energy differ by 250MeV, these events could be excluded from the further analysis. The remaining events are shown in figure 6.7.

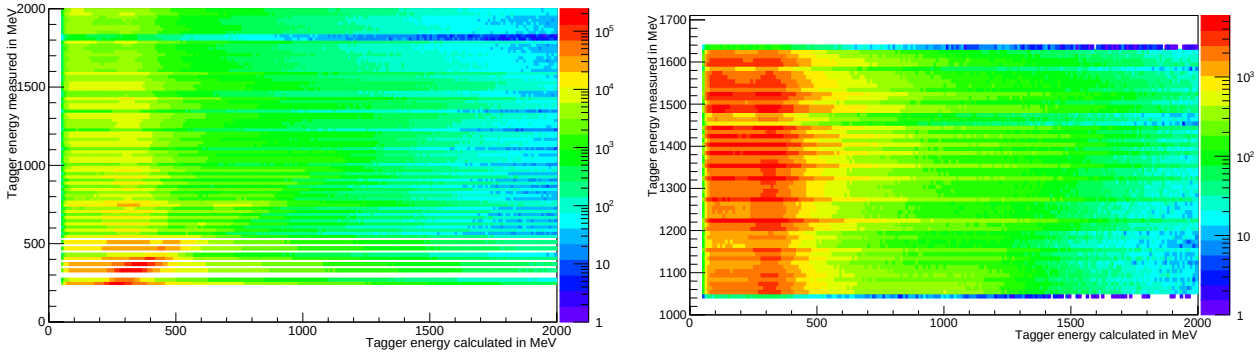

Figure 6.6: Measured vs calculated tagger photon energy, making use of the existing tagging system (left) or ARGUS (right).

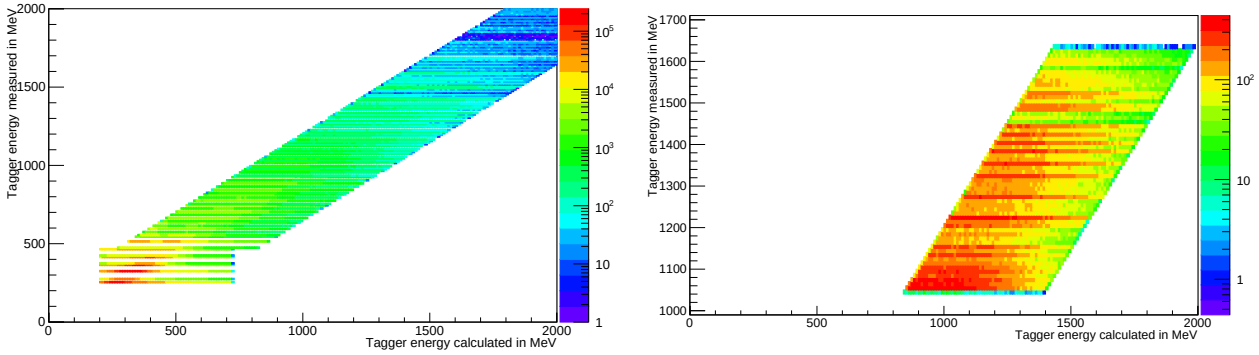

Figure 6.7: Measured vs calculated tagger photon energy after cut on diagonal entries with less then 250MeV difference between calculated and measured energy. Results for the existing tagging system (left) or ARGUS (right).

Since the ambiguity is not solved solely by applying this cut, in the next step, the missing mass is reconstructed using

$$m_{\mathrm{miss}} = \sqrt{\left(E_{\mathrm{photon}} + m_{\mathrm{target\ proton}} - E_{\mathrm{meson}}\right)^2 - \left(\vec{p}_{\mathrm{photon}} - \vec{p}_{\mathrm{meson}}\right)^2}. \tag{6.5}$$

In case of more than one electron in the trigger window, the one with the lowest difference between m_{miss} and m_{proton} is chosen as the best fitting one.

6.2.3 Selecting the best fitting proton

The same statement as for the tagger holds also for the protons. It is possible that two or more protons are detected in one trigger event. For this, the proton that fits best to the missing proton is selected. Best fitting is defined as the smallest difference in angle between proton and missing proton. If for one event protons are detected in more than one detector, the best fitting protons for them are compared to find the global best fitting proton. Figure 6.8 shows the impact of this selection method on the "missing mass versus invariant mass" plot. The background is heavily reduced up to one order of magnitude. Both plots show the results for the tagger since ARGUS covers only a small part of the photon energy spectrum.

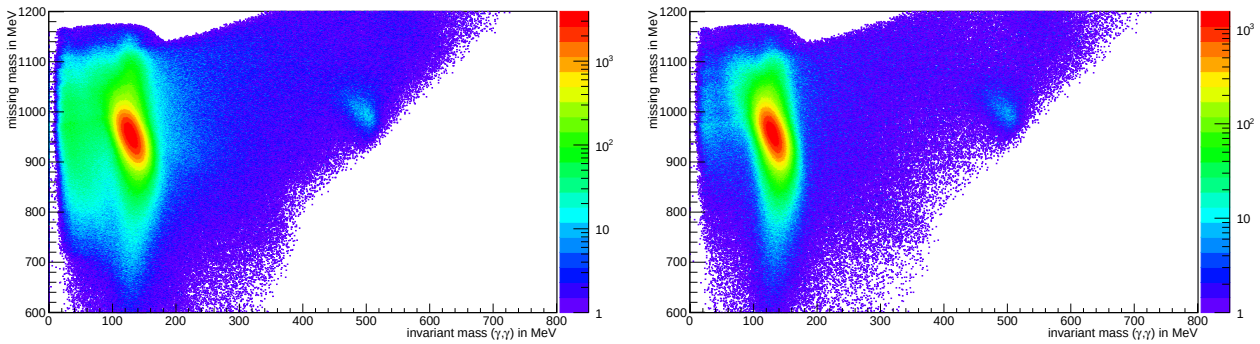

Figure 6.8: Missing mass versus invariant mass without reconstructed proton (left) and with reconstructed proton (right). The background can be reduced up to one order of magnitude. Both plots show the results for the existing tagger.

6.2.4 Cut on angle differences

The next step is to have a detailed look on the angle differences between the reconstructed proton and the missing one. Since at this point only the best fitting proton is selected this could still have a large difference in angle. To investigate this, the angle difference in Θ and Φ are plotted against each other as visible in figure 6.9. A two dimensional Gaussian is fitted to the datapoints to select the valid events in a 3σ region in both direction. The results for the existing tagger or ARGUS are:

$$\sigma_\Theta = 5.19 \pm 2.7 \cdot 10^-3 \qquad \sigma_\Theta = 4.91 \pm 1.6 \cdot 10^-2$$
$$\sigma_\phi = 5.37 \pm 2.3 \cdot 10^-3 \qquad \sigma_\phi = 4.75 \pm 9.6 \cdot 10^-3.$$

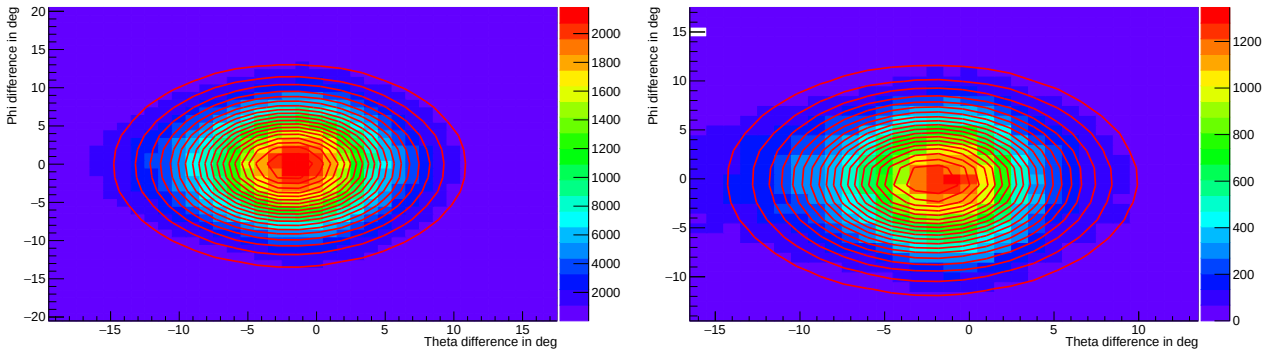

Figure 6.9: Angle differences in Θ and ϕ between reconstructed and missing proton. Results for the existing tagging system (left) or ARGUS (right). The red circles correspond to the two dimensional Gaussian fit.

6.2.5 Cut on π^0 mass and coplanarity cut

For the next event selection, the invariant mass in used. Figure 6.10 shows the invariant mass distribution of the 2γ-system with all previous cuts performed.

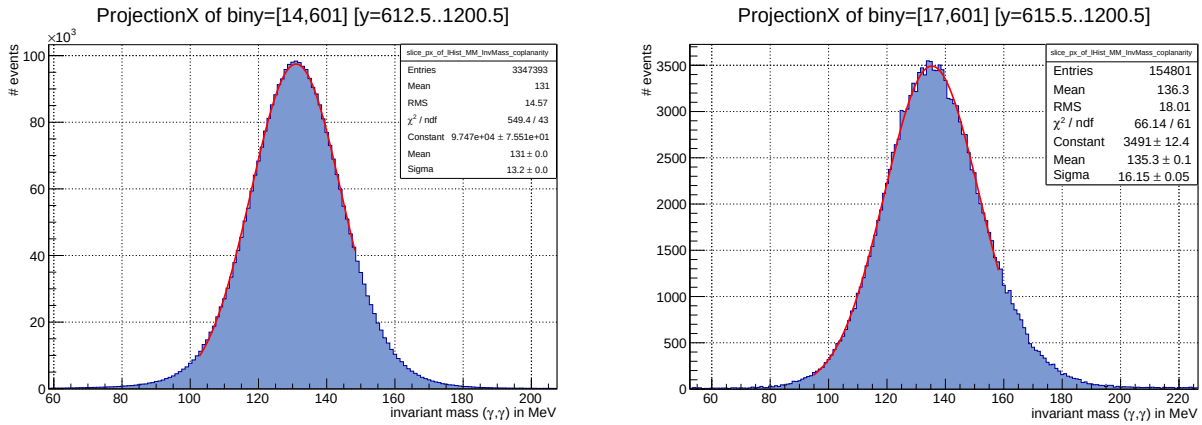

Figure 6.10: Invariant mass of the two photons inside the BGO. Results for the existing tagging system (left) or ARGUS (right).

A 3σ cut on the peak near the π^0 mass of 134.98MeV[PDG] is used for selecting π^0 events.

The π^0 reconstructed so far are now checked for coplanarity. Coplanarity means, that the π^0 and the proton are going back to back in ϕ direction in the lab frame. Figure 6.11 shows the measured values for the coplanarity together with the Gaussian fit. Since the initial transverse momenta are small, a value very close to 180° is expected.

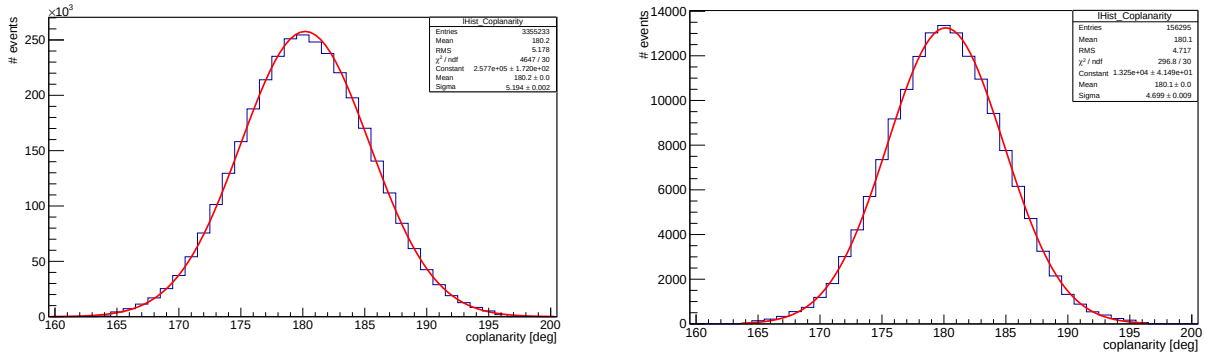

Figure 6.11: Coplanarity between π^0 and proton in ϕ direction. Results for the existing tagging system (left) or ARGUS (right).

6.2.6 Cut on calculated π^0 energy and missing mass

The last cuts performed to reduce the background, concern the reconstructed π^0 energy and the missing mass. The energy of the incoming tagger photon together with the reconstructed proton and π^0 angles are used to calculate the π^0-momentum, and then together with the reconstructed π^0-mass, to calculate the π^0-energy:

$$E_{\pi^0} = \sqrt{M^2_{\pi^0,rec.} + p^2_{\pi^0,rec.}}.$$

The value for the calculated π^0-energy is plotted against the difference in mass between the missing mass and the real proton mass of 938.27MeV[PDG]. A two dimensional Gaussian fit selects the valid events as

visible in figure 6.12. The fit results for the analysis performed with the existing tagger or ARGUS are:

$$\sigma_{E_{\pi^0}} = 52 \pm 5.5 \cdot 10^{-}5 \qquad \sigma_{E_{\pi^0}} = 54 \pm 1.3 \cdot 10^{-}3$$
$$\sigma_{\Delta M} = 47 \pm 2.6 \cdot 10^{-}5. \qquad \sigma_{\Delta M} = 49 \pm 1.1 \cdot 10^{-}3$$

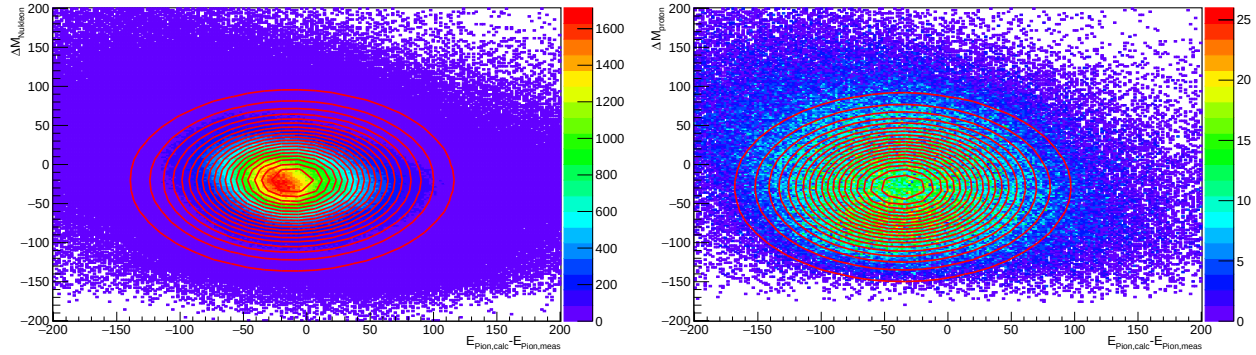

Figure 6.12: Reconstructed π^0 energy vs difference in missing mass to real proton mass. Results for the existing tagging system (left) or ARGUS (right).

6.3 Determining the degree of polarization $P_{\gamma,l}$

The degree of polarization can be extracted by splitting the reconstructed $\pi^0 p$ events, separated for both polarization planes, into energy, Θ_{CMS} and ϕ_{CMS} bins. For this analysis one bin in Θ_{CMS} and 12 in ϕ_{CMS} are used for each polarization plane. The energy range of $1300 - 1600$MeV was divided into 50MeV bins since the degree of polarization, that needs to be determined, depends on energy.

This procedure is performed individually for both polarization planes. By using equation

$$\frac{\overline{N}\left(\phi, \phi_{\gamma,l} = 45°\right) - \overline{N}\left(\phi, \phi_{\gamma,l} = -45°\right)}{\overline{N}\left(\phi, \phi_{\gamma,l} = 45°\right) + \overline{N}\left(\phi, \phi_{\gamma,l} = -45°\right)} = \Sigma P_{\gamma,l} \sin\left(2\phi\right) \tag{6.6}$$

with the ,to the integrated π^0 count rate normalized count rates $\overline{N}\left(\phi, \phi_{\gamma,l} = 45°\right)$ and $\overline{N}\left(\phi, \phi_{\gamma,l} = -45°\right)$ for the two polarization planes, the $\sin\left(2\phi\right)$[9] dependency is conspicuous in figure 6.13 for the energy bin $1400 - 1450$MeV. The left plot shows the results obtained with the tagger and the right one the results using only ARGUS. The errors for the datapoints are only statistical ones. The results for all energy bins can be found in appendix D. The fit function is given by:

$$f\left(\phi\right) = c_0 \cdot \sin\left(2\phi + p_1\right) + p_2 \tag{6.7}$$

The variable fit parameters are the amplitude c_0, a phase shift p_1 and an offset in y-direction p_2. They are shown in each plot in the corresponding box.

Since the amplitude in the shown plots is given by $\Sigma P_{\gamma,l}$ the degree of polarization can be determined with given values for Σ. Values for the beam asymmetry that are used for this, are obtained from MAID calculations [MAID]. Table 6.2 shows the results obtained with the existing tagger and ARGUS compared with the respective values given from calculation with the COBRIS program.

[9] The $cos\left(2\phi\right)$ becomes a $\sin\left(2\phi\right)$ due to the definition of the both polarization planes to be $\pm 45°$

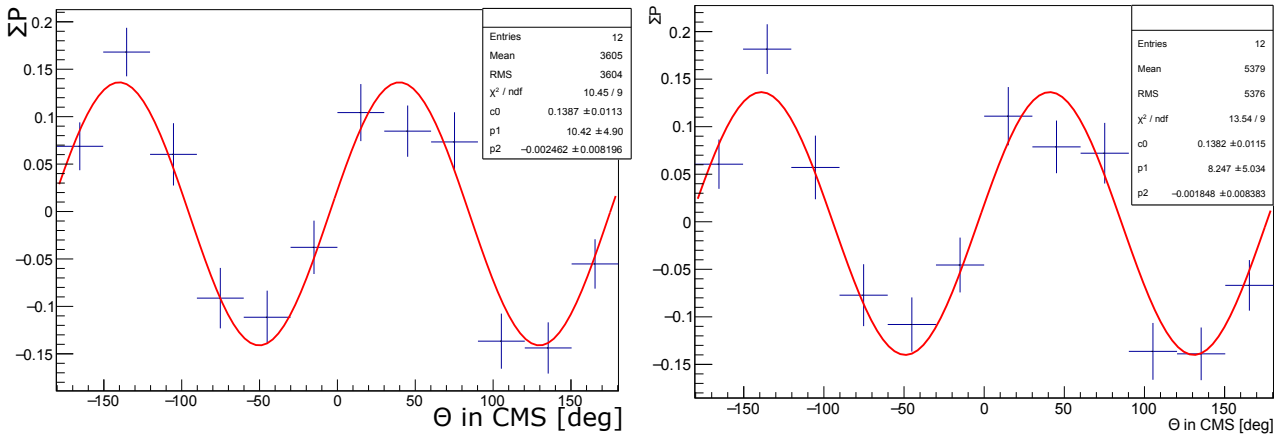

Figure 6.13: The $\sin(2\phi)$ modulation for energy bin $1400-1450$MeV. Results for the existing tagging system (left) or ARGUS (right).

energy bin [MeV]	degree of polarization $P_{\gamma,l}$ [%]			
	analysis tagger	COBRIS tagger	analysis ARGUS	COBRIS ARGUS
1300-1350	16.3 ± 3.1	18 ± 3	18.0 ± 3.2	16.8 ± 0.1
1350-1400	23.4 ± 2.4	21 ± 3	23.3 ± 2.5	19.3 ± 0.1
1400-1450	26.6 ± 2.2	24 ± 3	26.5 ± 2.2	22.3 ± 0.1
1450-1500	26.0 ± 2.7	26 ± 3	26.3 ± 2.8	24.4 ± 0.1
1500-1550	30.5 ± 2.6	28 ± 3	31.0 ± 2.6	24.7 ± 0.2
1550-1600	28.9 ± 3.5	25 ± 2	28.0 ± 3.7	21 ± 0.5

Table 6.2: Degree of linear polarization obtained through analysis of $\pi^0 p$ photoproduction compared with COBRIS determination. Errors are given trough the fits. For the analysis fits these are statistical errors while for the COBRIS calculation these are systematic ones.

The COBRIS program calculates the degree of polarization from the measured tagger or ARGUS spectrum. For detailed information about COBRIS see [Be].

The results show, that the improved energy resolution of ARGUS reduces the systematic error of the degree of polarization from calculations significantly compared to the tagger. This effect may reduce a bit when ARGUS is able to measure more than one coherent enhancement as the tagger does but still should be well pronounced.

The values for the polarization obtained from the analysis show a large agreement between the two detectors. The statistical error could be reduced towards previous measurements. Figure 6.14 shows first preliminary results from the beam asymmetry from a beamtime in November 2014 from Andreas Bella with large error bars due to a low statistic in this analysis.

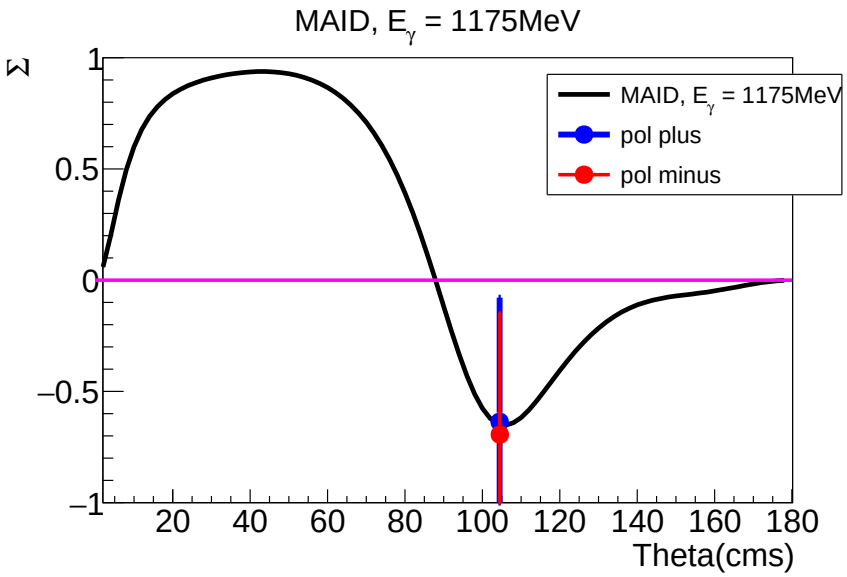

Figure 6.14: Previous measurements of the beam asymmetry performed by Andreas Bella.

The results for the analytic calculations and the analysis are comparable within the errorbars but nonetheless the value without error from the analytic calculations and differ slightly from the analysis for the tagger and even more for ARGUS. One reason is though to be small mistakes in the analytic calculations of the polarization for a collimated photon beam, which was used here. Also systematic uncertainties which will have an impact were not studied in this short analysis.

6.4 Analysis - Summary and Outlook

The short analysis of the beam asymmetry Σ performed with data obtained with the existing tagging system or ARGUS shows perfect agreements between both. The degree of polarization could be determined with an improved staticstic error compared to previous measurements. Also the comparison with the analytic calculations using the bremsstrahlungs spectrum delivered good results. Some minor changes of the analytic calculations are still needed but the results are already very close. Also an analysis of the systematic uncertainties that need to be performed very precisely. For a small crosscheck as performed with this analysis this is not necessary.
It was expected that ARGUS would reduce the systematic uncertainty of the calculated degree of polarization. This could be confirmed very clearly with a reduced uncertainty by one order of magnitude. If this still holds for measurements with the full detector, where more than only the first coherent enhancement is visible, it again shows that ARGUS is a success.

List of Figures

References

[AI] Autodesk Inventor, Product page, `http://www.autodesk.de/products/inventor/overview` (last checked: 01.10.15)

[Al15] ALEF, Stefan, *Scintillating fiber detector and kinematic fitting for the BGO-OD experiment*, Master thesis in physics, University of Bonn (2015)

[Be] Bella, Andreas, PhD thesis, in work

[Be03] S.-K. Choi et al. (Belle Collaboration), *Observation of a Narrow Charmoniumlike State in Exclusive* $B^{\pm} \to K^{\pm}\pi^{+}\pi^{-} J/\Psi$ *Decays*, Phys. Rev. Lett. 91, 262001 (2003)

[BGO] B1, Sonderforschungsbereich / Transregio 16, `http://bgo-od.physik.uni-bonn.de/` (last checked: 01.10.2013)

[BJ69] BJORKEN, J. D., *Asymptotic Sum Rules at Infinite Momentum.* In: Physical Review, vol. 179, Issue 5, pp. 1547-1553 (1969)

[CG69] CALLAN, C. G. Jr.; GROSS, David J. , *High-Energy Electroproduction and the Constitution of the Electric Current.* In: Phys. Rev. Lett. 22, 156 (1969)

[CH74] CHODOS, A.; JAFFE ,R. L.; JOHNSON, K.; THORN, C. B.; WEISSKOPF, V. F., *New extended model of hadrons.* In: Phys. Rev. D 9, 3471 (1974)

[CHT97] Chiang, W.-T.; Tabakin, F.; *Completness Rules for Spin Observables in Pseudoscalar Meson Photoproduction*, Physical Review D 34,2809-2835,1986

[EB12] EBERHARDT, Holger: *Bestimmung von Polarisationsobservablen in der* π^0 *und* ω *Photoproduktion am Proton mit dem CBELSA/TAPS-Experiment*, PhD thesis, University of Bonn (2012)

[ES33] ESTERMANN, I.; STERN, O., *Über die magnetische Ablenkung von Wasserstoffmolekülen und das magnetische Moment des Protons. II* In: Zeitschrift für Physik (01/1933), Volume 85, Issue 1-2, pp. 17-24

[FR15] FREYERMUTH, Oliver, *A new FPGA-based Time-over-Threshold System for the Time-of-Flight Detectors at the BGO-OD Experiment*, DPG Frühjahrstagung 2015, Heidelberg, 25. March 2015

[FS33] FRISCH, R.; STERN, O., *Über die magnetische Ablenkung von Wasserstoffmolekülen und das magnetische Moment des Protons. I* In: Zeitschrift für Physik (01/1933), Volume 85, Issue 1-2, pp. 4-16

[GE64] GELL-MANN, M, *A schematic model of baryons and mesons.* In: Phys.Lett. 8 (1964), pp. 214-215

[Ham1] H6568 Multianode Photomultiplier, Data sheet , `http://hep-www.px.tsukuba.ac.jp/~ukegawa/cpr/mapmt-16.pdf` (last checked: 01.10.15)

[Ham2] Hamamatsu, Home page, `http://www.hamamatsu.com/us/en/index.html` (last checked: 01.10.15)

[Hei54] HEITLER, W.: *The Quantum Theory of Radiation.* Oxford University Press, (1954)

[KDT95] Knochlein, G. ; Drechsel , D.; Tiator, L.: *Photo- and Electroproduction of Eta Mesons*, Z. Phys. A 352, 327-343, 1995

[Lan86] LANDAU, L.D ; LIFSCHITZ, E.M. Lehrbuch der theoretischen Physik, Band 4, Quantenelektrodynamik, Akademie-Verlag, (1986)

[LHCb15] LHCb Collaboration (Roel Aaij (CERN) et al.), *Observation of* $J/\Psi p$ *resonances consistent with pentaquark states in* $\Lambda_b^0 \to J/\Psi K^- p$ *decays.* In: Phys. Rev. Lett. 115, 072001 (2015)

[MAID] MAID homepage, Values for transverse polarization observables, `http://portal.kph.uni-mainz.de/MAID//maid2007/polariz.html` (last checked: 01.10.15)

[Mu13] MUCKHOFF, Verena, *Messung der Effizienz des Szintillator-Hodoskops für das BGO-OD Tagging-System*, Bachelor thesis in physics, University Bonn (2013)

[PDG] Particle Data Group, Particle property listings, `http://pdg.lbl.gov/2014/listings/contents_listings.html` (last checked: 01.10.15)

[PST96] PICHOWSKY, M. ; ŞAVKLI, Ç. ; TABAKIN, F.: *Polarization observables in vector meson photoproduction*, Physical Rev. C 53 (1996)

[SCH09] SCHMIEDEN, H.: *Photoproduction of ω-Mesons at ELSA and the Role of Azimuthal Asymmetries*, Chinese Physics C 33,1146-1152 (2009)

[SCHE15] SCHELUCHIN, Georg, *Meson photoproduction on the proton using the BGO-OD detector complemented by a new Scintillating Ring (SciRi)*, Master thesis in physics, University of Bonn (2015)

[SGo1] Saint Gobain, Scintillating fibers product page, `http://www.crystals.saint-gobain.com/Scintillating_Fiber.aspx` (last checked: 01.10.15)

[SGo2] Saint Gobain, Home page, `https://www.saint-gobain.com/en` (last checked: 01.10.15)

[SHKL11] SANDORFI, A.; HOBLIT, S.; KAMANO, H.;LEE, T.-S. H.: *Determining pseudoscalar meson photoproduction amplitudes from complete experiments*, Journal of Physics G: Nucl. Part. Phys. 38,2011

[Tim69] TIMM, U., *Coherent Bremsstrahlung of Electrons in Crystals.* In: Fortschritte der Physik 17 (1969), pp. 765Â–808

[Ue56] UEBERHALL, H., *High-Energy Interference Effect of Bremsstrahlung and Pair Production in Crystals* In: Phys. Rev. 103 (1956), pp. 1055-1067

[Wiki1] Wikipedia, *Scintillator* , `https://en.wikipedia.org/wiki/Scintillator` (last checked: 01.10.15)

[Wiki2] Wikipedia, *Photomultiplier* , `https://en.wikipedia.org/wiki/Photomultiplier` (last checked: 01.10.15)

[YU61] NE'EMAN, Y., *Derivation of strong interactions from a gauge invariance.* In: Nuclear Physics, Volume 26, Issue 2, Pages 222-229 (1961)

[ZW64] ZWEIG, G, *An SU3 model for strong interaction symmetry and its breaking.* In: Developments in the Quark Theory of Hadrons, pp.22-101, Version 1 is CERN preprint 8182/TH.401, Jan. 17, 1964

A Cross talk test results

P1	245	P5	2	P9	0	P13	0
P2	1	P6	1	P10	0	P14	0
P3	0	P7	0	P11	0	P15	0
P4	0	P8	0	P12	0	P16	0

Table A.1: Result for Pixel 1 not covered with tape.

P1	0	P5	0	P9	0	P13	0
P2	208	P6	0	P10	0	P14	0
P3	0	P7	0	P11	2	P15	0
P4	0	P8	1	P12	0	P16	0

Table A.2: Result for Pixel 2 not covered with tape.

P1	0	P5	0	P9	0	P13	0
P2	0	P6	0	P10	0	P14	0
P3	418	P7	0	P11	0	P15	0
P4	1	P8	0	P12	0	P16	0

Table A.3: Result for Pixel 3 not covered with tape.

P1	0	P5	0	P9	0	P13	0
P2	0	P6	0	P10	0	P14	0
P3	0	P7	0	P11	2	P15	0
P4	254	P8	0	P12	0	P16	0

Table A.4: Result for Pixel 4 not covered with tape.

P1	0	P5	262	P9	0	P13	0
P2	0	P6	1	P10	1	P14	0
P3	0	P7	0	P11	1	P15	0
P4	0	P8	0	P12	1	P16	0

Table A.5: Result for Pixel 5 not covered with tape.

P1	0	P5	0	P9	0	P13	0
P2	0	P6	467	P10	1	P14	0
P3	0	P7	0	P11	1	P15	0
P4	0	P8	1	P12	1	P16	0

Table A.6: Result for Pixel 6 not covered with tape.

P1	0	P5	0	P9	0	P13	0
P2	0	P6	0	P10	0	P14	0
P3	0	P7	546	P11	4	P15	0
P4	0	P8	0	P12	0	P16	0

Table A.7: Result for Pixel 7 not covered with tape.

P1	0	P5	0	P9	0	P13	0
P2	0	P6	1	P10	1	P14	0
P3	1	P7	2	P11	4	P15	0
P4	0	P8	375	P12	0	P16	0

Table A.8: Result for Pixel 8 not covered with tape.

P1	0	P5	0	P9	304	P13	3
P2	0	P6	1	P10	0	P14	0
P3	0	P7	0	P11	2	P15	0
P4	0	P8	0	P12	0	P16	0

Table A.9: Result for Pixel 9 not covered with tape.

P1	0	P5	0	P9	0	P13	0
P2	0	P6	1	P10	508	P14	0
P3	0	P7	0	P11	2	P15	0
P4	0	P8	0	P12	0	P16	0

Table A.10: Result for Pixel 10 not covered with tape.

P1	0	P5	0	P9	0	P13	0
P2	0	P6	0	P10	0	P14	0
P3	0	P7	1	P11	690	P15	1
P4	0	P8	0	P12	0	P16	1

Table A.11: Result for Pixel 11 not covered with tape.

P1	0	P5	0	P9	0	P13	0
P2	0	P6	2	P10	1	P14	0
P3	1	P7	2	P11	1	P15	0
P4	0	P8	0	P12	476	P16	0

Table A.12: Result for Pixel 12 not covered with tape.

P1	0	P5	0	P9	0	P13	345
P2	0	P6	0	P10	0	P14	0
P3	0	P7	0	P11	0	P15	0
P4	0	P8	0	P12	0	P16	0

Table A.13: Result for Pixel 13 not covered with tape.

P1	0	P5	0	P9	0	P13	0
P2	0	P6	0	P10	0	P14	378
P3	0	P7	0	P11	1	P15	0
P4	0	P8	0	P12	0	P16	0

Table A.14: Result for Pixel 14 not covered with tape.

P1	0	P5	0	P9	0	P13	0
P2	0	P6	0	P10	0	P14	0
P3	0	P7	0	P11	1	P15	281
P4	0	P8	0	P12	0	P16	0

Table A.15: Result for Pixel 15 not covered with tape.

P1	0	P5	0	P9	0	P13	0
P2	0	P6	0	P10	0	P14	0
P3	0	P7	0	P11	2	P15	0
P4	0	P8	0	P12	1	P16	384

Table A.16: Result for Pixel 16 not covered with tape.

B PMT properties

PMT number	cathod curr. $[\mu A/lm]$	anode curr. $[A/lm]$	anode dark curr. $[nA]$	Gain $[10^6]$	Voltage
3803	86.4	510	0.28	5.90	750
3773	83.8	403	0.05	4.81	760
3774	82.4	465	5.9	5.64	755
3767	88.6	687	0.61	7.75	725
3747	87.1	701	1.1	8.05	725
3743	85.7	554	1.6	6.46	745
3723	80.3	574	0.12	7.15	735
3679	89.5	631	0.71	7.05	735
3553	84.5	618	0.45	7.31	735
3569	80.5	379	0.01	4.71	760
3759	85.3	826	0.05	9.68	710
3751	95.0	834	5.7	8.78	720
3754	86.4	703	6.2	8.14	725
3745	92.4	789	1.4	8.54	720
3701	87.0	418	1.7	4.80	760
3728	83.9	460	5.5	5.48	755
3715	76.3	330	0.02	4.33	785
3700	87.5	568	0.33	6.49	745
3654	88.3	353	0.02	4.00	790
3652	88.5	379	0.03	4.28	785
3627	90.1	308	0.03	3.42	800
3590	97.1	322	0.06	3.32	800
3573	93.7	347	0.02	3.70	800
3572	93.2	308	0.01	3.30	800
3401	91.8	370	0.05	4.03	790
3917	85.7	466	0.26	5.44	755
3913	91.5	436	0.11	4.77	760
3911	87.5	620	1.8	7.09	735
3854	95.7	471	0.14	4.92	760
3915	84.2	420	0.09	4.99	760

Table B.1: Properties of PMTs.

C Scatches and real pictures of ARGUS

C.1 second prototype

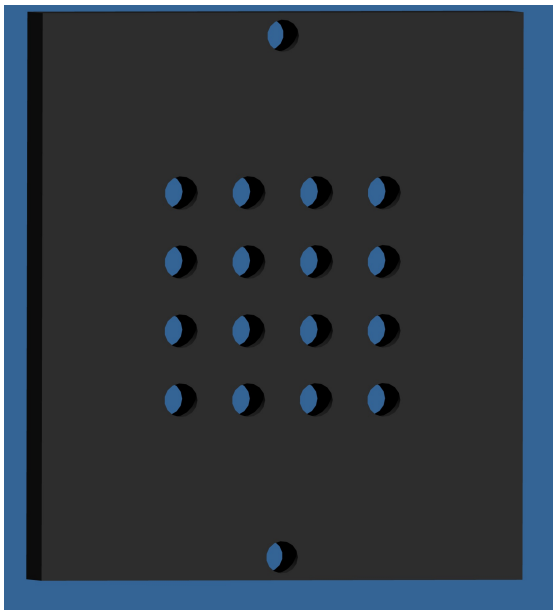

Figure C.1: PVC fiber holder of the second prototype.

C.2 final design

Figure C.2: pictures of ARGUS final setup during and after construction.

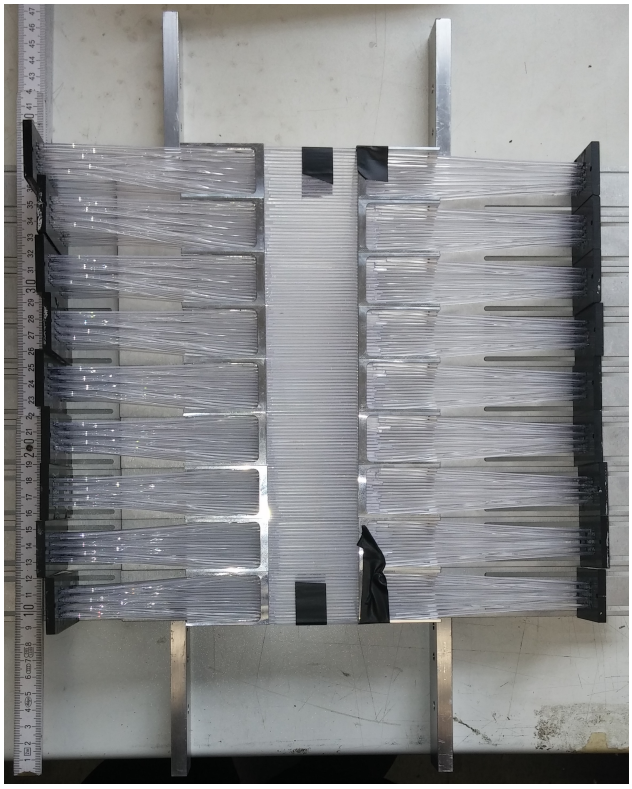

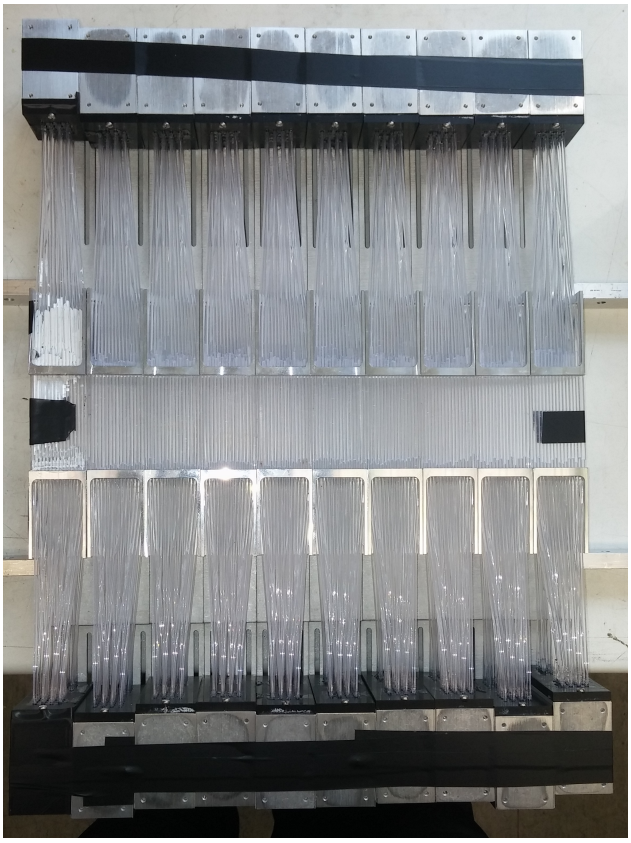

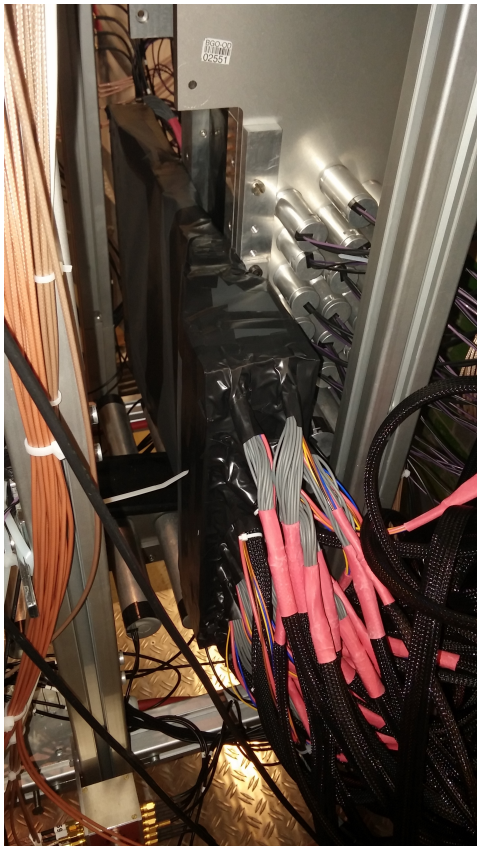

Figure C.3: pictures of ARGUS final setup during and after construction.

D Asymmetry plots

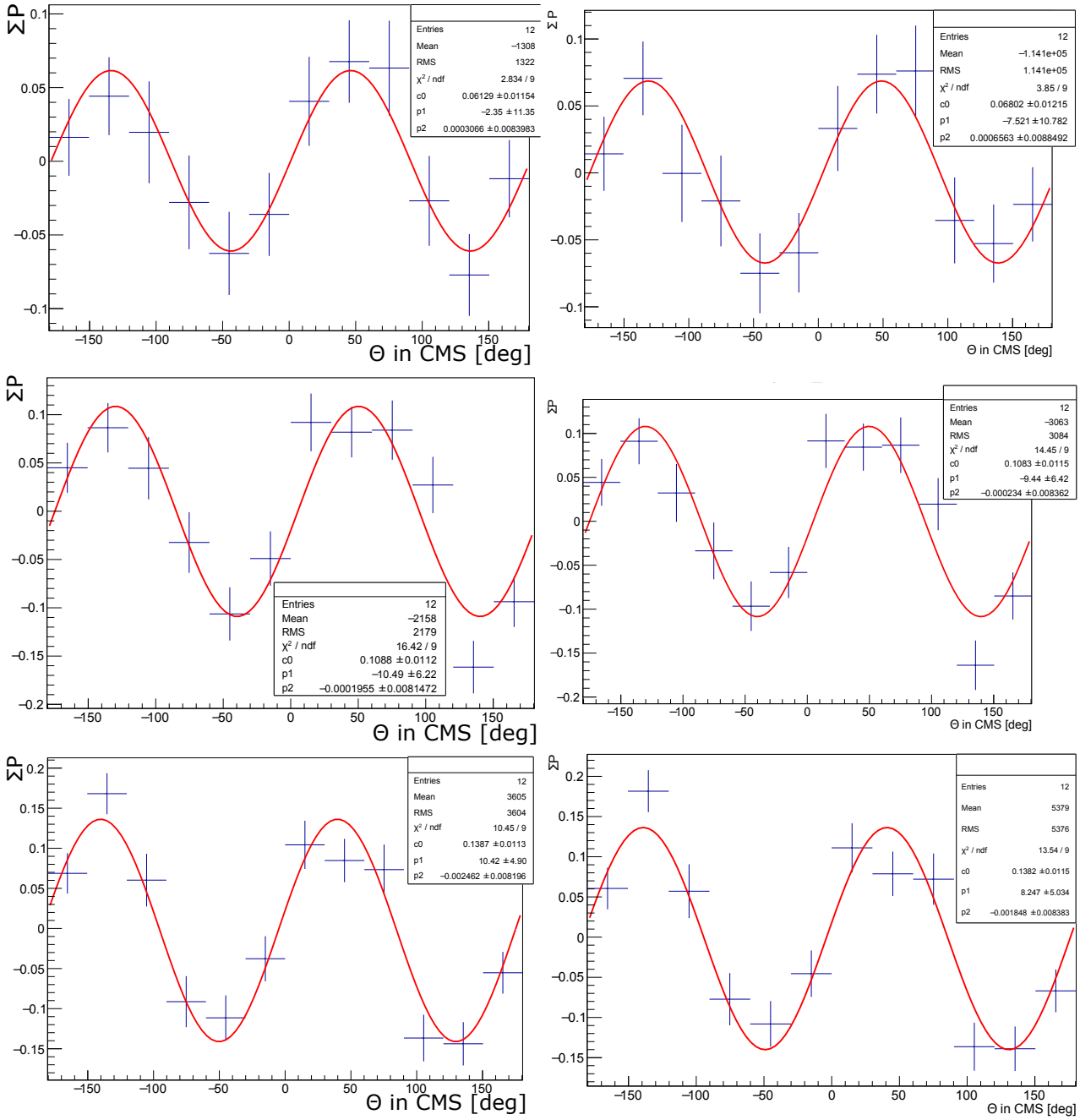

Figure D.1: $\sin(2\phi)$ modulation for the energy range of $1300 - 1600$MeV seperated in 50MeV bins. Energy increasing from top to bottom plot. Results for the existing tagging system (left) or ARGUS (right).

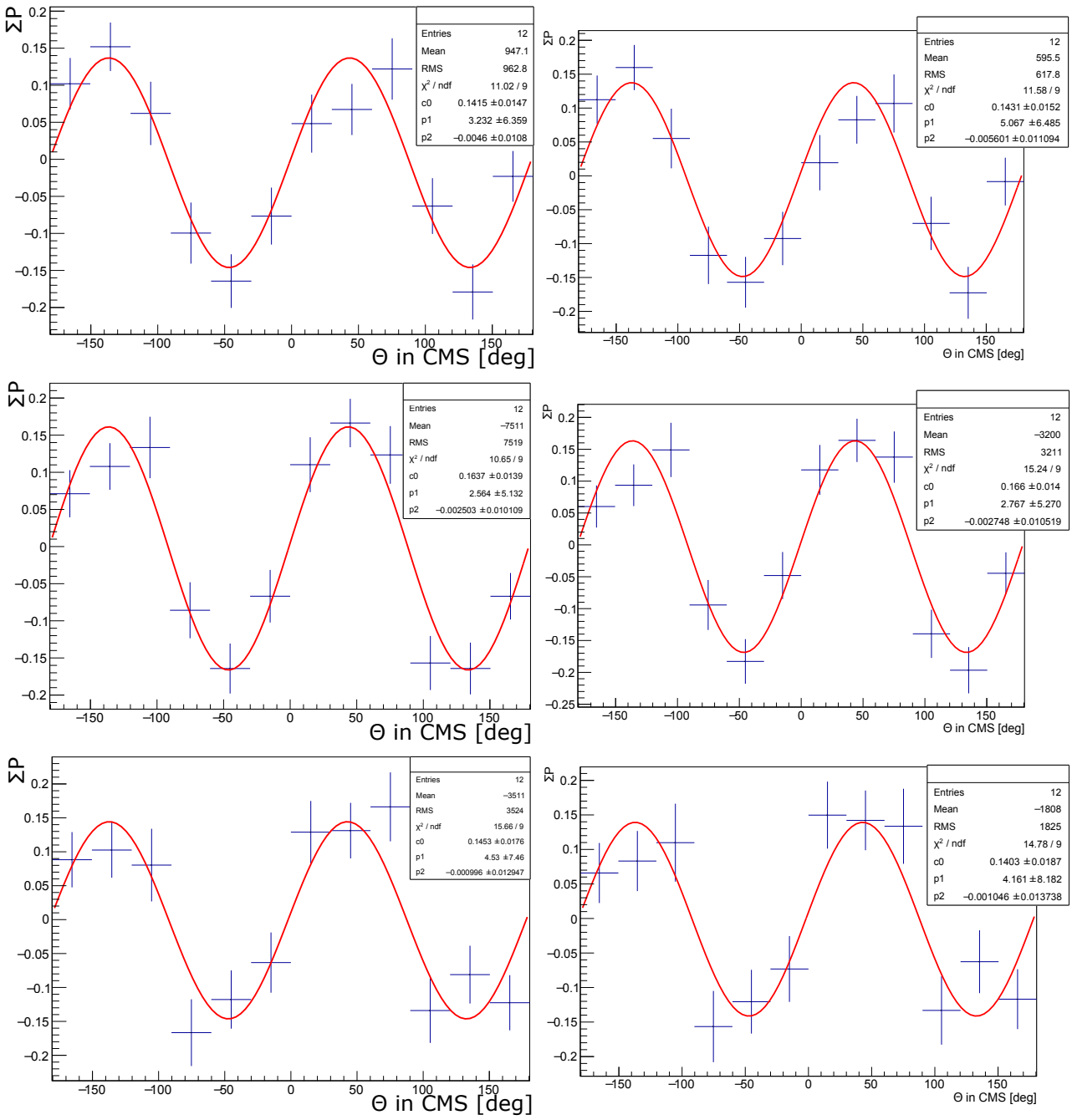

Figure D.2: $\sin(2\phi)$ modulation for the energy range of $1300 - 1600$MeV seperated in 50MeV bins. Energy increasing from top to bottom plot. Results for the existing tagging system (left) or ARGUS (right).

Acknowledgments

I would like to thank Prof. Dr. Hartmut Schmieden for giving me the opportunity to work in his group and to be a part of the BGO-OD experiment. I also thank Prof. Dr. Philip Cole for his cooperation in our work on ARGUS especially concerning discussions and feedback. I want to thank all the members of the work group of Prof. Schmieden for help, discussions, feedback or just entertaining chats. Especially Andreas Bella and Tom Jude have my thanks for helping me with the analysis part.

I am also very glad that I had the chance to work together with Stefan Alef on ARGUS. I was an interesting and awesome time.

Zu guter letzt möchte ich mich herzlichst bei meiner Familie und meinen Freunden bedanken, die mir all die Jahre zur Seite standen, und mich zu dem Menschen gemacht haben der ich heute bin.

I hereby declare that the work presented here was formulated by myself and that no sources or tools other than those cited were used.

Bonn, ...

date signature